6-11-2015

Star Formation and Quenching Among the Most Massive Galaxies at $z \sim 1.7$

C. Mancini
INAF - Osservatorio Astronomico di Padova, Italy

A. Renzini
INAF - Osservatorio Astronomico di Padova, Italy

E. Daddi
CEA-Saclay, France

G. Rodighiero
Universitá di Padova, Italy

S. Berta
Max-Planck-Institut für Extraterrestrische Physik (MPE), Germany

See next page for additional authors

Right click to open a feedback form in a new tab to let us know how this document benefits you.

Follow this and additional works at: https://uknowledge.uky.edu/physastron_facpub

Part of the Astrophysics and Astronomy Commons, and the Physics Commons

Authors

C. Mancini, A. Renzini, E. Daddi, G. Rodighiero, S. Berta, N. Grogin, Dale D. Kocevski, and A. Koekemoer

Star Formation and Quenching Among the Most Massive Galaxies at $z \sim 1.7$

Star formation and quenching among the most massive galaxies at $z \sim 1.7$

C. Mancini,[1,2]$\star$ A. Renzini,[1] E. Daddi,[3] G. Rodighiero,[2] S. Berta,[4] N. Grogin,[5] D. Kocevski[6] and A. Koekemoer[5]

[1]*INAF - Osservatorio Astronomico di Padova, Vicolo dell'Osservatorio, 5, I-35122 Padova, Italy*
[2]*Dipartimento di Fisica e Astronomia 'Galileo Galilei', Universitá di Padova, Vicolo dell'Osservatorio, 3, I-35122 Padova, Italy*
[3]*CEA-Saclay, Service dAstrophysique, F-91191 Gif-sur-Yvette, France*
[4]*Max-Planck-Institut für Extraterrestrische Physik (MPE), Postfach 1312, D-85741 Garching, Germany*
[5]*Space Telescope Science Institute, 3700 San Martin Drive, Baltimore, MD 21218, USA*
[6]*Department of Physics and Astronomy, University of Kentucky, Lexington, KY, 40506, USA*

ABSTRACT

We have conducted a detailed object-by-object study of a mass-complete ($M_* \geq 10^{11} \, \mathrm{M_\odot}$) sample of 56 galaxies at $1.4 \leq z \leq 2$ in the Great Observatories Origins Deep Survey-South field, showing that an accurate deblending in 24 µm images is essential to properly assign to each galaxy its own star formation rate (SFR), whereas an automatic procedure often fails. This applies especially to galaxies with SFRs below the main sequence (MS) value, which may be in their quenching phase. After that, the sample splits evenly between galaxies forming stars within a factor of 4 of the MS rate ($\sim$45 per cent), and sub-MS galaxies with SFRs $\sim$10–1000 times smaller ($\sim$55 per cent). We did not find a well-defined class of intermediate, transient objects below the MS, suggesting that the conversion of a massive MS galaxy into a quenched remnant may take a relatively short time (<1 Gyr), though a larger sample should be analysed in the same way to set precise limits on the quenching time-scale. X-ray detected AGNs represent a $\sim$30 per cent fraction of the sample, and are found among both star-forming and quenched galaxies. The morphological analysis revealed that $\sim$50 per cent of our massive objects are bulge-dominated, and almost all MS galaxies with a relevant bulge component host an AGN. We also found sub-MS SFRs in many bulge-dominated systems, providing support to the notion that bulge growth, AGN activity and quenching of star formation are closely related to each other.

Key words: galaxies: evolution – galaxies: formation – galaxies: high-redshift – galaxies: structure.

1 INTRODUCTION

The transition from a star-forming regime to passive evolution, that we call *quenching*, is perhaps the most important event that may happen to a galaxy in the course of its life. Yet, the physical processes causing quenching are still poorly understood, making this a main frontier issue in galaxy evolution. We know that the first quenched (massive) galaxies appear at redshifts $\sim$2–3 (e.g. Cimatti et al. 2004; Williams et al. 2009; Gobat et al. 2012; Cassata et al. 2013) and that their fraction and number density increase steadily with cosmic time, to the point that they come to dominate the stellar mass in galaxies in the local Universe (e.g. Baldry et al. 2004). We also know that the quenched fraction increases steeply with galaxy mass independently of local environment, as well as with local environmental overdensity, independently of their mass. We

therefore speak of *mass quenching* and *environment quenching* as two distinct, *separable* processes (Peng et al. 2010b, 2012). Yet, the physical nature of such processes is still merely conjectural and it has also been suspected that they could be different manifestation of a same underlying process (Carollo et al. 2014; Knobel et al. 2015).

The probability (or relative frequency) of mass quenching appears to increase exponentially with stellar mass (M_*), or almost indistinguishably with the star formation rate (SFR), given the tight SFR–M_* correlation that exists for *main sequence* (MS) galaxies (Daddi et al. 2007a; Elbaz et al. 2007; Noeske et al. 2007; Schreiber et al. 2015). A variety of radically different options are currently entertained for the mass quenching process, whereby quenching is either an *internal* or an *external* process. In one option for the former case sudden energy/momentum release from star formation and/or AGN (feedback) results in the ejection of all gas from galaxies that then turn passive, the 'quasar mode' quenching in current jargon (e.g. Granato et al. 2004). Powerful AGN jets may also heat

$\star$ E-mail: chiara.mancini@oapd.inaf.it

the circumgalactic medium to high temperature thus preventing further accretion of cold gas, the so-called radio mode AGN feedback (Croton et al. 2006). In another option for an external process, the circumgalactic gas is shock-heated to high temperatures as the mass of the host dark matter halo (M_h) exceeds a critical threshold (of order of $\sim 10^{12}\,M_\odot$), and therefore it stops to cool and flow into the galaxy, thus discontinuing to feed star formation (e.g. Birnboim & Dekel 2003). Finally, the growth of a central mass concentration (bulge) may *quench itself*, with increasing shear (differential rotation) suppressing the disc instability to form actively star-forming clumps, the so-called gravitational (or morphological) quenching (Martig et al. 2009; Genzel et al. 2014a). So, we have at least four options for the physical nature of mass quenching. Moreover, the tight correlations existing between halo mass, stellar mass, bulge mass and mass of the central black hole make difficult to disentangle between these options, as all result in a correlation of the quenched fraction with galaxy mass (Peng et al. 2012). In other words, it is not clear whether the pertinent mass in mass quenching is M_* or M_h, or the mass of the central bulge (Lang et al. 2014), or even the mass of the central black hole.

The frequency of AGN activity is found to increase strongly with galaxy mass, especially at $z \gtrsim 1$ (Reddy et al. 2005; Daddi et al. 2007b; Fiore et al. 2008; Brusa et al. 2009; Bongiorno et al. 2012; Mullaney et al. 2012a,b; Cimatti et al. 2013; Förster Schreiber et al. 2014; Genzel et al. 2014b; Perna et al. 2015; Rodighiero et al. 2015), which provides circumstantial support for a connection between AGN feedback and mass quenching. However, finding the smoking gun of AGN quenching proved to be very difficult, as most AGNs are hosted by actively star forming galaxies showing no signs of being quenched. Actually, the mere galaxy-AGN *co-evolution* concept argues for both growing and be quenched together. On the other hand, supermassive black holes (SMBH) do not grow in one shot. Rather, a galaxy may experience many nuclear activity cycles interleaved with inactive phases (Novak, Ostriker & Ciotti 2012; Hickox et al. 2014), with the former ones leading to feedback and driving nuclear outflows, but failing to quench. Hence, if AGN quenching really works, not every AGN cycle leads to quenching but just a final, fatal one. Later, once star formation is quenched by ejecting the gas, so is the nuclear activity as well. This AGN variability on a variety of time-scales clearly makes the connection AGN-quenching difficult to unambiguously recognize (Hickox et al. 2014).

While mass quenching works equally for satellites and centrals, environment quenching appears to be exclusive of satellite galaxies (Peng et al. 2012), but see also Knobel et al. (2015). Also for the physics of environment quenching various options exist. Ram-pressure stripping is one possibility (Gunn & Gott 1972), perhaps favoured by the finding that the quenched fraction of satellites correlates better with the local overdensity inside groups than with group richness, a proxy for the mass of the host halo (Peng et al. 2012). But other options include strangulation (Larson, Tinsley & Caldwell 1980) and harassment (Moore et al. 1996).

In the Peng et al. phenomenological model, mass quenching starts promptly at relatively high redshifts and, of course, acts preferentially on massive galaxies. Environment quenching sets in progressively, becomes more important at lower redshifts, following the growth of overdensities and large-scale structures.

In this paper, we focus on mass quenching, and to do so we deal only with the most massive galaxies, namely those with $M_\star \geq 10^{11}\,M_\odot$. We then explore the relatively narrow redshift range $1.4 \leq z \leq 2$, because this corresponds to an epoch when mass quenching has started to work at full steam, while environmental

quenching is just about to begin.[1] All such massive star-forming galaxies must soon start to be quenched, otherwise – keeping to form stars at the MS rate – would soon result in a dramatic overgrowth of their mass (Renzini 2009; Peng et al. 2010b). So, all such galaxies are almost immediate precursors to quenched, passively evolving, red and early-type galaxies (ETG). Thus, a mass selection $M_* \geq 10^{11}\,M_\odot$ of galaxies at the mentioned redshifts ensures that it will include only galaxies which are either already quenched, or being in the course of quenching, or that will soon (i.e. $\lesssim 10^9$ yr) enter the quenching phase.

Such mass and redshift range has been already widely explored by many observational studies using large data bases, in particular trying to address the quenching issue (e.g. Wuyts et al. 2011; Barro et al. 2013; Williams et al. 2014). Some of these studies deal with very large numbers of galaxies to ensure the statistically significant samples that are crucial to understand the global trends of galaxy evolution. Given the sheer size of the samples, automated methods are used to derive a few fundamental parameters for each galaxy, such as SFR, mass, structural parameters etc. As such, not all information present in the data could be used. We then restrict ourselves to work, intensively rather than extensively, on a quite small sample of galaxies, examining them one by one. The purpose is first to unambiguously distinguish between galaxies which are forming stars at the MS rate, those which are already quenched, and those which appear to be still star forming, but at a rate significantly below the MS, which may be caught in the *quenching* phase. We also aim to investigate possible links between galaxy specific star formation rate (sSFR), morphology, AGN activity. The presence of a well-known overdensity at $z \simeq 1.61$ in the GOODS-S field (Castellano et al. 2007; Kurk et al. 2009; Giavalisco et al. 2011) also allows us to check the relative abundance of quenched galaxies, bulge-dominated galaxies, and AGNs within and outside the overdensity.

The paper is organized as follows. Section 2 describes the sample selection and the used catalogues and data sets. In Sections 3, we derive galaxy stellar mass and SFR and define the M_*–SFR MS at $1.4 \leq z \leq 2$, used as reference throughout all the paper. AGN hosts are discussed in Section 3.3. In Section 4, galaxies are classified in quenched or star forming, based on their position relative to the MS, multiwavelength information, colours, and SED-fitting analysis. In Section 5, we perform morphological analysis based on single- and double-component surface brightness (SB) fitting, and separately treat some peculiar system. Based on our results, we discuss the role of the AGN activity, and of the environment, in quenching star formation in Sections 6, and 7, respectively. Section 8 presents the conclusions. Throughout the paper, we assume a Λ cold dark matter cosmology with $H_0 = 70\,\mathrm{km\,s^{-1}\,Mpc^{-1}}$, $\Omega_M = 0.27$, and $\Omega_\Lambda = 0.73$. All stellar masses and SFR are quoted for a Salpeter (1955) initial mass function (IMF), and magnitudes are given in the AB photometric system, unless explicitly stated otherwise.

2 DATA AND SAMPLE SELECTION

The relatively small field (10 arcmin × 16 arcmin) of the Great Observatories Origins Deep Survey-South (GOODS-S; Giavalisco et al. 2004) represents the optimal choice for studying in detail a representative sample of the most massive galaxies at $1.4 \leq z \leq 2$.

---

[1] For example, in the case of the Peng et al. (2010b) phenomenological model at $z \sim 2$ and $M* = 10^{11}\,M_\odot$ the mass quenching rate is over two orders of magnitude higher than the environment quenching rate, see their fig. 13.

In fact, it provides at the same time both high-resolution images in the near-IR with WFC3/*HST* (CANDELS; Grogin et al. 2011; Koekemoer et al. 2011), and the deepest data in the mid-IR (*Spitzer*; Rieke et al. 2004), far-IR(*Herschel*, PEP/HerMES; Elbaz et al. 2011; Lutz et al. 2011), and X-ray band (*Chandra* Deep Field-South, CDF-S; Xue et al. 2011). The corresponding data base is crucial to study the optical rest-frame morphology, accurately estimate the SFR for the most massive objects (most of which are highly obscured by dust), and to unveil X-ray excess due to the AGN contribution. Last but not least, the large amount of ground-based (VLT) and space-based (*HST*, *Chandra*, *Spitzer*) data from the GOODS Treasury Program, and the availability of spectroscopic redshifts from the GOODS and GMASS programs (Vanzella et al. 2005; Cimatti et al. 2008; Popesso et al. 2009; Kurk et al. 2013) enable us to character-ize the studied galaxies in an optimal way as currently possible. Of course, the resulting sample will be too small for coping with statis-tics or cosmic variance, but this is not a limitation in our *intensive* approach.

In this work, we focus on the 56 most massive ($M_* \geq 10^{11}$ M$_\odot$) galaxies at $1.4 \leq z \leq 2$, 31 of which have spectroscopic redshifts. Two more objects entered the original sample, but they have been excluded from this study, because their WFC3/*HST* images are not available, or too noisy to perform SB fitting, due to the proxim-ity of saturated stars. The sample was culled from the *K*-selected (*K*(Vega) < 22) multiband catalogue of Daddi et al. (2007a, here-after D07), including data from all the available filters in GOODS-S, i.e. *HST*/ACS optical, *F435W* (*B*), *F606W* (*V*), *F775W* (*I*), and *F850LP*(*z*), VLT/ISAAC near-IR, *J*, *H*, *K*, and *Spitzer*/Infrared Ar-ray Camera (IRAC), 3.6, 4.5, 5.8, and 8.0 μm (for more details on the data sets see Giavalisco et al. 2004). The optical/near-IR photom-etry was then complemented with the 24 μm catalog (Daddi et al., in preparation), built as summarized in Section 2.1 from the Multi-Band Imaging Photometer for Spitzer (MIPS) images (Rieke et al. 2004). Far-IR fluxes were extracted (Daddi et al., in preparation) from the publicly released PACS 70–160 μm data from *Herschel* GOODS (Elbaz et al. 2011), and SPIRE 250 μm data from Herschel Multi-tiered Extragalactic Survey (HerMES; Oliver et al. 2010). For objects without spectroscopic information, we used photometric redshifts from the public GOODS-MUSIC catalogue, which agree well with the spectroscopic ones ($\Delta z/(1 + z) \simeq 0.03$) for galaxies at *z* < 2 (cf. Grazian et al. 2006, 2007). Although the uncertainties on photometric redshifts could result in the inclusion in the sample of a few lower redshift contaminants, we avoided applying colour criteria to pre-select high-*z* objects, in favour of completeness. The *HST*/WFC3/*F160W* *H*-band image mosaic (>5σ point source sen-sitivity for H_{160} < 27.7, AB system) drizzled to a pixel scale of 0.06 arcsec, was exploited to study galaxy morphology in the op-tical rest frame with a very high resolution (FWHM ∼ 0.18 arcsec $\simeq$ 1.5 kpc). For more details on the observations and data reduction see Grogin et al. (2011) and Koekemoer et al. (2011).

2.1 MIPS fluxes

The MIPS source extraction on the whole GOODS-S MIPS/24 μm image mosaic will be described in a future paper (Daddi et al., in preparation). Here, we briefly summarize the main issues, useful for the purpose of this work. The 24 μm/MIPS counterparts were identified, based on the IRAC (3.6 μm) prior positions, using a point spread function (PSF) fitting method, with GALFIT (version 3; Peng et al. 2010a). The measurement errors were calibrated on direct Monte Carlo simulations, inserting one artificial source at a time in the real image, and measuring it together with all other priors.

The catalogue was built in such a way that a MIPS flux, or a flux upper limit, in case of MIPS-undetection, is associated with each IRAC source. The use of IRAC priors helps with the deconfusion of objects blended in MIPS, but is still biased against sources which are also blended in IRAC. In the D07 catalogue, IRAC sources are associated with the *K*-band coordinates using an encircling radius of 2.0 arcsec. However, when the angular separation between the IRAC and *K*-band positions is $\Delta\theta_{K-IRAC} > 0.5$ arcsec, the galaxy is probably blended in IRAC (cf. D07), and generally disregarded. Since objects with $\Delta\theta_{K-IRAC} > 0.5$ arcsec represent a not negligible fraction in our sample (i.e. 6/56), we used prior positions from *HST*/WFC3/*F160W* to deblend them, as described in Section 4 and Appendix A.

We considered as MIPS-detection all sources with S/N $\geq$ 3 (i.e. detected above 3σ). For undetected sources, we derived upper lim-its from the flux errors at 2σ or 3σ, for sources with S/N < 1 and 1 $\leq$ S/N < 3, respectively. In Fig. 1, we compare our results with those from the catalogue of Magnelli et al. (2009, hereafter M09). The figure shows the ratio between the MIPS fluxes from our catalogue and those from the M09 catalogue (F24/F24(M09)) as a function of F24(M09). For sources undetected in M09, we estimated 2σ or 3σ flux upper limits as we did for objects in our catalogue. With one exception, all the sources detected in our catalogue are also detected in M09 and are shown as red filled circles in Fig. 1. For sources undetected in both catalogues the black arrows show the corresponding upper limits in F24(M09) and the vertical axis show the ratio of the upper limits in the two catalogues. The excep-tion, object #5530, is shown as a red arrow. The red (black) shaded histogram show the corresponding distributions of flux ratios (of the ratio of upper limits) for detected (undetected) sources. Gaussian fits to the histograms, shown as dot–dashed lines, give a mean (μ) and standard deviation (σ) as $\mu \pm \sigma = 1.06 \pm 0.14$, and 1.21 ± 0.74, for detected, and undetected sources, respectively. The comparison shows that for sources detected above 3σ, the 24 μm/MIPS fluxes are in general agreement with those from M09. On average, also the upper limits are in fair agreement between the two catalogues,
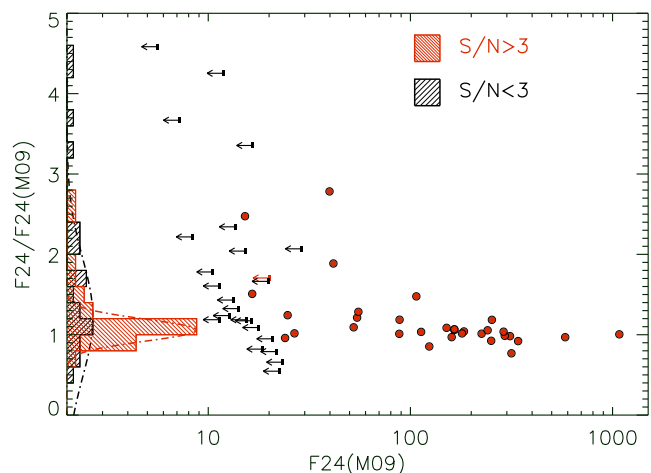

Figure 1. The ratio between our 24 μm/MIPS fluxes (F24; Daddi et al. in preparation) and those from M09 (F24(M09)), as a function of F24(M09). For undetected sources (S/N < 3), we plot 2σ or 3σ flux upper limits, as detailed in the text. Objects detected (undetected) in both catalogues are shown as red filled circles (black arrows). The object #5530 detected in our catalogue, but undetected in M09, is shown as a red arrow. The red and black shaded histograms (scaled down to arbitrary units), show the distributions of sources which are detected and undetected in our catalogue, respectively. Gaussian fits to the histograms are shown as red and black dot–dashed lines.

whereas for a small number of objects our upper limits are more conservative.

3 THE MAIN SEQUENCE (MS) OF STAR-FORMING GALAXIES AT ⟨z⟩ = 1.7

It is now well established that a tight relation exists between the stellar mass ($M_\star$) and the SFR for star-forming galaxies, both in the local Universe and at high redshift (D07; Elbaz et al. 2007; Noeske et al. 2007; Pannella et al. 2009; Karim et al. 2011; Rodighiero et al. 2014; Schreiber et al. 2015). At all redshifts the majority of star-forming galaxies follow this relation within a $\lesssim 0.3$ dex dispersion with a small fraction of outliers (cf. Rodighiero et al. 2011), thus it is commonly called the MS of star-forming galaxies. While the slope of the SFR–$M_\star$ relation does not change much with redshift, its zero-point, i.e. the specific SFR (sSFR = SFR/M_*) at fixed mass gradually increases with redshift at least up to $z \sim 2.5$ (Wuyts et al. 2011; Sargent et al. 2012; Whitaker et al. 2012). At higher redshifts, it is still debated whether the sSFR remains constant or keeps (slightly) increasing (González et al. 2010, 2014; Béthermin et al. 2013; Stark et al. 2013; de Barros, Schaerer & Stark 2014). So, massive galaxies at high redshifts formed stars and grew their mass at a much faster rate, fuelled by a larger reservoir of fresh gas, with respect to local galaxies (Daddi et al. 2010; Tacconi et al. 2010).

To study our sample galaxies as a function of their position on the $M_\star$–SFR diagram, we define here the MS of star-forming galaxies at ⟨z⟩ ≈ 1.7, to be used as a reference in quantifying as sSFR/sSFR(MS) the deviation from it of any given galaxy. We adopted the following empirical relation from Béthermin et al. (2012), based on the Sargent et al. (2012) parametrization of the sSFR evolution with redshift for MS galaxies, which in turn is derived by fitting a combination of mid-IR, UV, far-IR, and radio data:

$$\mathrm{sSFR_{MS}}(z, M_*) = \mathrm{sSFR_{MS,0}} \times \left(\frac{M_\star}{10^{11}\,\mathrm{M_\odot}}\right)^{\beta_{\mathrm{MS}}} \times (1+z)^{\gamma_{\mathrm{MS}}}, \tag{1}$$

where $\mathrm{sSFR_{MS,0}} = 0.063\,\mathrm{Gyr^{-1}}$ is the sSFR at $z = 0$ for $M_\star = 10^{11}\,\mathrm{M_\odot}$, $\beta_{\mathrm{MS}} = -0.21$ is the slope of the sSFR–$M_\star$ relation derived by Rodighiero et al. (2011), and $\gamma_{\mathrm{MS}} = 3$ describes the evolution of the normalization of the MS out to redshift $z = 2.5$. All these parameters are given in Béthermin et al. (2012, table 1) assuming a Salpeter (1955) IMF. From equation (1) it follows that the MS at ⟨z⟩ ≈ 1.7 is given by

$$\log \mathrm{SFR} = -6.6 + 0.79 \log M_*. \tag{2}$$

3.1 Stellar mass

The stellar masses were computed based on the *K*-band magnitudes, according to the empirical relation derived in Daddi et al. (2004, hereafter D04) and D07 (with a typical error of a factor of ∼2), for homogeneity with the samples used to derive the reference MS (i.e. Rodighiero et al. 2011; Béthermin et al. 2012; Sargent et al. 2012), in which stellar masses were derived using this method. In D04, the empirical relation was tested and calibrated on the results from best-fitting spectral energy distributions (SED) of Fontana et al. (2004), using Bruzual & Charlot (2003, hereafter BC03) stellar population models, and Salpeter IMF. As shown in Section 4.2, we verified that the stellar masses derived with this method ($M_{\star\mathrm{D04}}$) agree well with those obtained from the SED fitting analysis (i.e. $M_{\star\mathrm{SED}}$) also for our massive sample.

3.2 Star formation rate

By combining the deep PACS *Herschel* data with all the high-quality multiband information at shorter wavelengths, we estimated SFRs including both the contribution of the UV rest frame (from the unobscured part of the light), and of the total IR emission, i.e. the light reprocessed by dust. The total SFR is then indicated as

$$\mathrm{SFR(IR + UV)} = \mathrm{SFR(IR)} + \mathrm{SFR(UV)}. \tag{3}$$

Following Kennicutt (1998), we inferred the UV contribution (SFR(UV)), from the 1500 Å rest-frame luminosity (L_{1500}), which in turn was derived from the observed *B*-band magnitude, as done in D07.

The IR contribution, SFR(IR), was derived from the total IR luminosity integrated over the full infrared spectrum, i.e. rest frame L[8–1000 μm] (hereafter LIR) using the Kennicutt (1998) conversion, for a Salpeter IMF (i.e. SFR(IR) = $1.7 \times 10^{-10}\,\mathrm{M_\odot\,yr^{-1}\,L_\odot^{-1}}$). LIR was measured by fitting the *Spitzer*/MIPS and *Herschel*/PACS/SPIRE photometry (i.e. from 24 μm to 250 μm) to the SED templates for MS galaxies at $z = 1.325$–2.25 from Magdis et al. (2012). The possible contribution of an obscured AGN was also taken into account in the fit, as in Rodighiero et al. (2011). The uncertainties on LIR were estimated from the χ^2 variations following Avni (1976) for the case of one single parameter. This is a robust method to retrieve the LIR when a galaxy is detected in at least two filters (i.e. MIPS/24 μm and one *Herschel* filter). Otherwise, it only provides an upper limit to LIR. Hence, the LIR of objects detected in MIPS, but undetected in *Herschel*, was estimated based on the 8 μm rest-frame luminosity ($L8 = \nu L_\nu[8\,\mu\mathrm{m}]$), according to the empirical relation proposed by Elbaz et al. (2011):

$$\mathrm{LIR} = L8 \times 4.9^{+2.9}_{-2.2}, \tag{4}$$

where 1σ errors on the coefficient are indicated. For galaxies in the considered redshift range ($z = 1.4$–2) the 8 μm rest-frame luminosity can be derived from the observed MIPS/24 μm flux (F_{24}), with a relatively small *k-correction* depending on the redshift ($0.8 \lesssim k_{\mathrm{corr}}(z) \lesssim 1.9$), as:

$$L8 = \nu_{24\,\mu\mathrm{m}}\,F_{24}\,4\pi DL(z)^2\,k_{\mathrm{corr}}(z), \tag{5}$$

where *DL(z)* is the Luminosity distance. The *k-correction* was derived using the Magdis et al. (2012) templates for MS galaxies at $z = 1.325$–2.25. For MIPS-detected/PACS-undetected objects, we verified that the MIPS-derived LIRs are consistent with the 2σ upper limits derived from the IR SEDs.

For objects undetected in MIPS, upper limits to the LIR, and correspondingly SFR(IR), were estimated from the MIPS/24 μm detection-limit (i.e. accurately measured on the MIPS images, as described in Section 2.1), using equations (4) and (5). We ignore here a possible contribution to LIR coming from circumstellar dust in old stellar populations, which may be relevant for sub-MS galaxies. Hence, for such galaxies, the resulting SFR(IR+UV) should be regarded as an upper limit, while a better constraint on the SFR can be derived from optical/near-IR SED fitting (see Section 4.2).

3.3 Identification of AGN hosts

We cross-correlated our sample with both the 4 Ms *Chandra* X-ray catalogue (Xue et al. 2011), and the VLA (1.4 GHz) radio catalogue (Miller et al. 2008), using an encircling radius of 1.0 arcsec, and found 19 and 5 counterparts, respectively (cf. Table 1). All the radio-detected objects are also X-ray detected, at least in one of the three bands of the 4 Ms *Chandra* catalogue (i.e. Soft: 0.5–2 kev,

Table 1. Massive Sample: multiwavelength and spectroscopic information from GOODS/CDFS/CANDELS surveys.

ID	RA (deg)	DEC (deg)	z	zq[1]	Ref[2]	F_{24} (μJy)	$F_{24,\rm new}$ (μJy)	$F_{\rm 1.4GHz}$[3] (μJy)	$F_{\rm Hard-X}$[4] ($10^{-16}\frac{\rm erg}{\rm cm^2\,s}$)	L_X[4] ($10^{42}\frac{\rm erg}{\rm s}$)	class(X)/(o)[5]	sub-sample
282	53.061 039	−27.693 52	1.44	0	b, CaHK	<17.22						MIPS-u
427	53.173 473	−27.697 678	1.427	1	b, CaHK-MgII-Mg	155.19 ± 10.64	<17.66					MIPS-d→u
428	53.173 6946	−27.698 1106	1.59	0		<31.92	<21.01[8]					MIPS-u
552	53.141 1934	−27.701 1375	1.604	1	a	66.1 ± 6.02			<4.2	11.0±3.2	AGN	MIPS-d
557	53.176 3992	−27.701 1547	1.981	1	a	24.89 ± 6.73						MIPS-d
686	53.104 889	−27.705 238	1.617	1	d	564.94 ± 19.92	423.76 ± 11.71	88.5 ± 14.6	27.0±1.7	77.0±2.1	QSO-1/BLAGN	PACS-d
687	53.104 6181	−27.705 4272	1.609	1	b	<59.76						MIPS-u
720	53.062 0193	−27.706 501	1.89	0		<28.23	204.38 ± 9.41		3.8±1.6	8.9±3.3	AGN	MIPS-u→d
848	53.108 5548	−27.710 1555	1.609	1	a	<18.75[6]						MIPS-u
856	53.183 0406	−27.709 0015	1.76	0		23.02 ± 7.37						MIPS-d
880	53.149 6506	−27.711 3838	1.612	1	a	30.7 ± 6.0	<41.55					MIPS-d→u
887	53.179 775	−27.711 674	1.416	1	a	<19.34						MIPS-u
903	53.089 447	−27.711 5822	1.72	0		242.9 ± 14.82			<3.4	5.7±1.5	AGN	PACS-d
947	53.116 4207	−27.712 7037	1.61	1	a	<19.78[6]						MIPS-u
986	53.151 2337	−27.713 728	1.609	1	a	<18.75[7]						MIPS-u
1084	53.152 7634	−27.716 2361	1.614	1	a	<12.33[6]						MIPS-u
1187	53.127 9221	−27.718 8625	1.66	0	a	37.61 ± 6.55	<19.18[6]					MIPS-d→u
1272	53.130 501	−27.721 18	1.415	1	a	<25.76[6]						MIPS-u
1510	53.188 858	−27.725 603	1.618	0		305.44 ± 16.63						MIPS-d
1906	53.045 4712	−27.737 5183	1.613	1	c	289.09 ± 16.27		3312.0 ± 13.3	95.0±2.9	240.0±4.0	QSO-1/BLAGN	PACS-d
2450	53.174 6445	−27.753 3722	1.848	1	a	<15.35						MIPS-u
2470	53.027 4162	−27.753 8891	1.63	0		71.05 ± 18.29						PACS-d
2940	53.141 0179	−27.766 7179	1.903	1	b, MgII	<17.61[6]			<1.2	1.8±0.7	AGN	MIPS-d
3066	53.165 5693	−27.769 8498	1.55	2	b, OII-(MgII)	227.82 ± 14.21	<41.66		28.0±1.7	60.0±2.2	AGN	PACS-d
3230	53.043 789	−27.774 668	1.615	2	c	110.77 ± 9.46						MIPS-d→u
3231	53.044 9028	−27.774 3626	1.61	1	c	78.47 ± 15.55	<46.43		<2.2	4.4±0.9	AGN	MIPS-d→u
3236	53.078 1097	−27.774 2271	1.729	1	c	254.29 ± 15.24	<19.06[6]					PACS-d
3258	53.052 1927	−27.774 7669	1.605	1	c	<19.06[6]			2.0±0.8	4.9±1.3	AGN	MIPS-u
3853	53.125 061	−27.790 7791	1.553	1	c, MgII-AlII(red)	27.15 ± 7.42	<13.43[6]					MIPS-u
4310	53.044 6396	−27.805 4123	1.61	0		<13.43[6]						PACS-d
4406	53.101 093	−27.808 559	1.97	0	b, [OII]-D4000	116.99 ± 8.68						PACS-d
4705	53.066 715	−27.816 507	1.413	1		174.75 ± 11.67		169.8 ± 12.5	<1.2	<1.0		MIPS-d
5149	53.171 7644	−27.825 676	1.74	0		<19.18						MIPS-d
5415	53.067 7795	−27.832 0599	1.79	0		57.23 ± 7.51						MIPS-d
5503	53.157 2495	−27.833 5114	1.619	1	b, OII(noisy)	232.03 ± 14.39			<1.2	1.1±0.5	AGN?	PACS-d
5509	53.057 8232	−27.833 4866	1.65	0		<18.38[7]			5.7±0.8	39.0±3.6	AGN	MIPS-u
5530	53.047 6723	−27.835 022	1.51	0		34.12 ± 8.19	<34.68[6]		2.5±0.6	3.3±0.4	AGN	MIPS-d→u
5534	53.072 67	−27.834 1789	1.616	1	b, [OII](faint)	313.95 ± 16.8						PACS-d
5556	53.150 166	−27.834 509	1.612	1	b, [OII]-MgII	<31.10						MIPS-u
5564	53.127 1667	−27.834 5394	1.81	0		<15.28[6]						MIPS-u
5860	53.131 4774	−27.841 2781	1.613	1	b, OII-MgII	191.47 ± 12.52		58.8 ± 12.8	1.2±0.5	2.1±0.7	AGN	PACS-d
5974	53.071 64	−27.843 6356	1.9	0		176.35 ± 11.75						PACS-d
6071	53.198 8525	−27.843 8873	1.57	0		299.89 ± 16.52			12.0±1.6	38.0±4.6	AGN	MIPS-d
6193	53.076 344	−27.848 677	1.536	0	d	158.05 ± 10.79			62.0±2.8	170.0±7.2	AGN-2/HEX	MIPS-d
6224	53.137 0697	−27.850 0233	1.45	0		105.85 ± 8.17						PACS-d
6352	53.060 07	−27.852 9701	1.544	1	d	89.08 ± 7.43			6.6±1.1	15.0±2.2	AGN-2/HEX	PACS-d

Table 1 – *continued*

ID	RA (deg)	DEC (deg)	$zq^{(1)}$	z	$Ref^{(2)}$	F_{24} (µJy)	$F_{24,\,new}$ (µJy)	$F_{1.4GHz}^{(3)}$ (µJy)	$F_{Hard-X}^{(4)}$ ($10^{-16}\frac{erg}{cm^2\,s}$)	$L_X^{(4)}$ ($10^{42}\frac{erg}{s}$)	$class(X)/(o)^{(5)}$	sub-sample
6572	53.077 282	−27.859 5829	0	1.96		299.89 ± 16.52						PACS-d
6647	53.168 438	−27.861 8145	0	1.77		<32.90$^{(6)}$						MIPS-u
6898	53.157 3715	−27.870 0867	1	1.603	e	1085.15 ± 25.54		112.7 ± 12.7	98.0±2.8	250.0±3.7	QSO-1/HEX	PACS-d
7077	53.208 0154	−27.874 3706	1	1.609	b	104.89 ± 8.13						MIPS-d
7116	53.182 4493	−27.875 3071	0	1.48		163.92 ± 11.1						PACS-d
7491	53.148 407	−27.885 511	0	1.604		<12.27$^{(6)}$						MIPS-u
7617	53.099 564	−27.890 564	0	1.57		<18.21$^{(6)}$						MIPS-u
7923	53.079 632	−27.901 369	0	1.4		<50.40	<17.12$^{(6)}$					MIPS-u
8121	53.211 2389	−27.908 2909	0	1.81		<15.71$^{(6)}$			<4.8	4.8±1.6	AGN	MIPS-u
8569	53.121 048	−27.928 5126	1	1.469		182.92 ± 12.09						MIPS-d

(1) Redshift quality flag: 0 = photometric, 1 = spectroscopic, likely (in agreement within 68 per cent confidence limits with the photometric redshift).
(2) References for spectroscopic redshifts: (a)GMASS (KurK et al. 2012), (b)FORS2 (v3.0, Vanzella et al. 2008), (c)K20 (Mignoli et al. 2005), (d)X-ray CDFS (Szokoly et al. 2004), (e)VIMOS (Popesso et al. 2009; Balestra et al. 2010).
(3) VLA Radio integrated flux Data from Kellermann et al. (2008), ATCA survey, Norris et al. (2006), and Afonso et al. (2006).
(4) Data from 4 Ms *Chandra* X-ray catalogue (Xue et al. 2011): Flux Hard-X band(2–8 kev), and total integrated Full-band (0.5–8 kev) luminosity.
(5) Objects identified as AGN, based on X-ray/Radio data as explained in Section 3.3. X-ray/Optical classification from Szokoly et al. (2004) is also reported, when available: class(X) = X-ray class (AGN-1,2, or QSO-1,2); class(o) = classification only based on optical spectra (HEX = object with unresolved emission lines and exhibiting high ionization lines, or emission line ratio indicating AGN activity. These objects are dominantly optical type-2 AGNs or QSOs; BLAGN = objects with emission lines broader than 2000 km s^{-1}. This classification implies an optical type-1 AGN or QSO).
(6) 2σ upper limits in MIPS for objects with a S/N <1 (3σ upper limits are used for the remaining objects).
(7) Marginal MIPS detection, i.e. 2.5<S/N<3, treated as 3σ upper limit.
(8) This galaxy has been classified as MIPS-u, being very likely a lens system, whose MIPS flux (Flux(24 µm)$_{new}$ = 152.12 ± 7.0), derives from a background source at likely z ∼ 2–2.5 (see Appendix A).

Hard: 2–8 kev, and Full: 0.5–8 kev). All the X-ray-detected objects in our sample had been classified as 'AGN candidates' by Xue et al. (2011). However, we considered as AGN hosts only those galaxies showing an excess in X-ray and/or radio luminosity with respect to the expected SFR, derived by summing the UV- and the IR-derived contributions, i.e. SFR(IR+UV). We used the Mineo et al. (2014) calibration, relating the total, integrated X-ray luminosity LX[0.5–8 kev] to the galaxy SFR (LX/SFR = (4.0 ± 0.4) × 10^{39} [erg s^{-1}/ M$_\odot$ yr^{-1}]), and found that all the X-ray detected galaxies, but two (i.e. #4705, and #5503) show an X-ray excess (at least by a factor of 3). In a similar way, by adopting the conversion of Ivison et al. (2010a,b), we verified that all our radio-detected galaxies (#686, #3231, #5503, #5860, and #5898) have a higher radio-emission (by a factor of >2.5) than what expected only from star formation, thus revealing the AGN contribution. Since #5503 shows radio excess, but no X-ray excess, we consider this object just as an AGN candidate. We notice that this source also exhibits a peculiar, asymmetric, morphology, and a large offset (∼1 arcs) between the optical and the X/radio positions, indicating that it could be a merging system. In the following figures, it will be flagged with a different symbol (large circle + four-pointed star) with respect to the other more secure AGNs, just marked as four-pointed stars. Based on the LX-SFR(IR+UV) comparison, object #4705 is instead considered as a normal star-forming galaxy. We conclude that 18 X-ray detected AGNs (17 secure, and one candidate) are included in our massive sample (see Table 1). This roughly corresponds to ∼ 30 per cent of the galaxies with $M_* \geq 10^{11}$ M$_\odot$ at $1.4 \leq z \leq 2$ in GOODS-S. Interestingly, we will show in the following that AGN hosts are not only among star-forming galaxies, but they represent ∼ 22 per cent of the quenched sources.

4 SOURCE CLASSIFICATION

4.1 Position on the M_*–SFR plane

The position occupied by our massive galaxies in the SFR–M_* plot is shown in Fig. 2. The MS relation at $\langle z \rangle = 1.7$, derived from equation (2), is bounded by two dashed lines, representing offsets in SFR 4 times above and 4 times below the MS following Rodighiero et al. (2011), and roughly corresponding to the ∼2.5σ dispersion. Here, and throughout all the paper, the sample is colour-coded based on the galaxy IR properties. Blue filled circles are objects detected at *Herschel* (PACS) wavelengths, and hereafter are indicated as the PACS-d sub-sample. Sources detected at 24 µm/MIPS, but not detected by *Herschel*, hereafter the MIPS-d galaxies, are shown as green filled circles and have, on average, a lower sSFR compared to the previous sub-sample. Then, objects which are not detected above 3σ at 24 µm/MIPS (i.e. $F\nu_{24} \lesssim$ 20–25 µJy, on average) are indicated as MIPS-u galaxies, and the corresponding upper limits on their SFR are shown as red filled circles. Thus, this sub-sample should include quenched systems, or galaxies with a low residual of star formation. The 17 secure AGN hosts identified in Section 3.3 are highlighted by four-pointed stars, and the AGN candidate by a four-pointed star+circle. For comparison, we also show the parent sample of 24 µm/MIPS-detected star-forming galaxies at $1.4 \leq z \leq 2$, for which the IR contribution to the SFR(IR+UV) was derived from equations (4), and (5) (black open circles).

As mentioned in Section 2.1, for completeness, we also included in our sample the objects with $\Delta\theta_{K-IRAC} > 0.5$ arcsec, which are blended in IRAC and, consequently, in MIPS. A close examination of *HST* and MIPS maps for all the 56 galaxies then revealed that
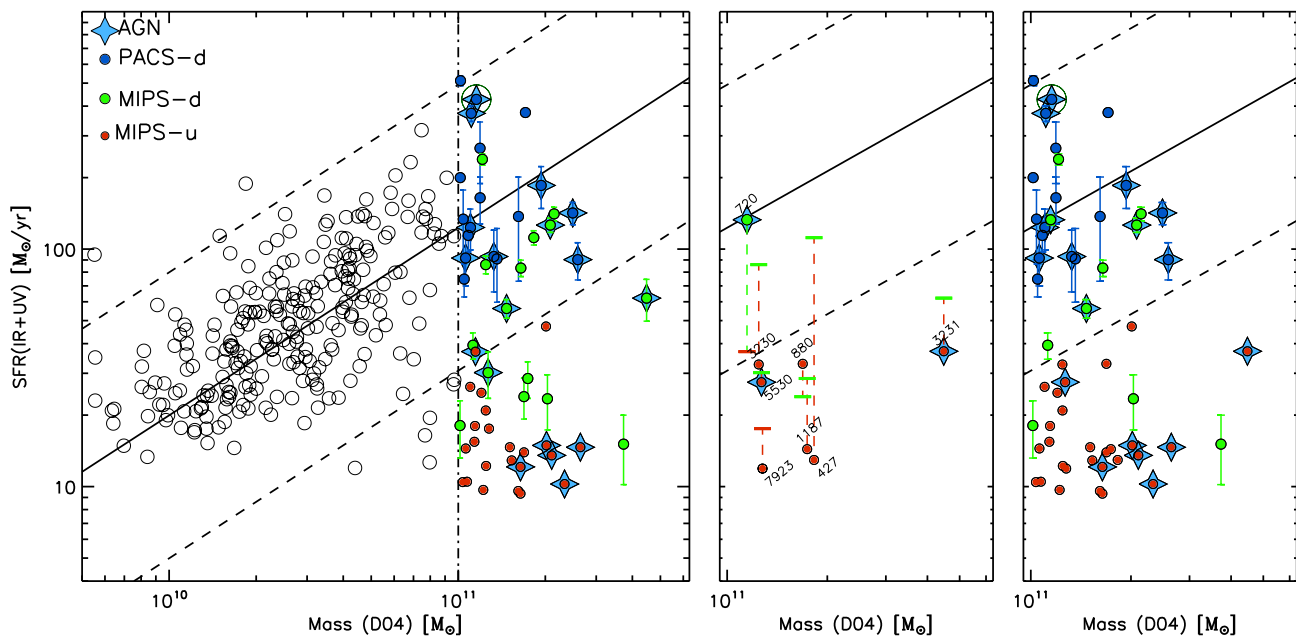
Figure 2. In this figure, we show the position of our massive sample galaxies on the MS at ⟨z⟩ = 1.7 (black solid line), before (left-hand panel) and after (right-hand panel) MIPS-deblending procedure (see Appendix A). In the central panel, we report the 'migration path' of each deblended galaxy, from the position occupied before (horizontal bar, colour-coded as the object in the left-hand panel), and after deblending (filled circle, colour-coded as the object in the right-hand panel). The right-hand panel shows the final positions with respect to the MS. The PACS-d, MIPS-d, and MIPS-u galaxies are displayed with different colours, as labelled in the figure, and explained in the text (Section 4). Note that the red filled circles just represent 2σ, or 3σ upper limits to the SFR for MIPS-u galaxies (cf. Section 2.1, and 4.1). For comparison, lower-mass star-forming galaxies at $1.4 \leq z \leq 2$, and detected at 24 μm/MIPS, from the parent sample, are shown the as black open circles.

six other objects are blended and could have been misclassified (i.e. as MIPS-d or MIPS-u) by the automatic procedure associating the MIPS sources to *K*-selected counterparts. Most of them reside in projected (or real) galaxy pairs, and in many cases both objects in a pair are included in our massive sample (see Appendix B). Hence, we attempted to deblend these objects to derive a more accurate estimate of their SFR, and re-classify them as MIPS-detected or undetected, if necessary, as briefly summarized below and further detailed in Appendix A).

We used GALFIT to fit PSF models to the 24 μm maps with the *F*160*W*/WFC3 positions as priors, leaving the galaxy magnitude as the only free parameter to be recovered. This procedure worked quite smoothly in most cases but some 'ambiguous' objects are discussed in Section 4.3.1. In the right-hand panel of Fig. 2, we show the final SFR–M_* diagram obtained after MIPS deblending, while in the middle panel we show the 'migration path' of each deblended galaxy from the position occupied before deblending (horizontal bar, colour-coded as in the left-hand panel) and after deblending (filled circle, colour-coded as in the right-hand panel). The 'migration path' is also colour-coded depending on the sub-sample to which the object belong after deblending (e.g. migrations from the MIPS-d to the MIPS-u sub-sample are drawn in red, and vice versa in green). From Fig. 2, it appears that several galaxies, previously classified as MIPS-d, have been reclassified as MIPS-u objects after deblending (MIPS-d→u in Table 1). This is the case for objects: #427, #880, #1187, #3230, #3231, and #5530. On the contrary, only galaxy #720, previously indicated as MIPS-u, has been reclassified as MIPS-d (MIPS-u→d). Then, object #7923 is confirmed to be a MIPS-u galaxy, but with a lower limit on its 24 μm flux, hence on its SFR. The deblending procedure for each object is detailed in Appendix A.

All the PACS-d galaxies are within the MS band, while all the MIPS-u galaxies are more than 4 times below it. The MIPS-d sub-class instead includes objects both on, and below the MS. Hence, some of the MIPS-d galaxies could be quenching, or even quenched systems, judging from the relatively wide range that they cover in sSFR (10^{-9}–$10^{-10.4}$ yr^{-1}, i.e. from the typical MS rate down to ∼20 times lower). It is also possible that some MIPS-d galaxy is instead undergoing a sort of rejuvenation process, caused by a merging/accretion event, although we expect that most such massive high-z galaxies are evolving in the opposite direction. Finally, in some case the observed MIPS emission could be powered not (only) by star formation, but (also) by obscured AGN, AGB stars, or old stellar population (Salim et al. 2009).

In the following sections (cf. Section 4.2, 4.3, and 4.3.1), we combined the IR/X/radio information with the results from SED fitting, and two-colour diagrams to better constrain the SFR of our galaxies and shed some light on the nature of some ambiguous objects.

4.2 SED fitting

We built the multicolour SEDs by fitting the optical to IRAC/8 μm photometry using the HYPERZMASS software (Bolzonella, Miralles & Pelló 2000; Pozzetti et al. 2007). For IRAC-blended objects, we excluded the IRAC bands from the fit. However, we verified that the best-fitting parameters do not change substantially using instead the IRAC fluxes from Guo et al. (2013), which are deblended with the template-fitting method (TFIT) procedure. For galaxies at $1.4 \leq z \leq 1.7$, the 8 μm flux was excluded from the SED fit, as at those redshifts it corresponds to a rest frame part of the spectrum that may include thermal dust and 3.3 μm PAH emission line, features which are not included in the used stellar population models. We

adopted BC03 stellar population models, with a grid of star formation histories (SFH) including an simple stellar population (SSP), a constant SFR, and exponentially declining τ-models (τ=0.1, 0.3, 1, 2, 5, 10, 15, and 30 Gyr). To reduce the number of free parameters, we only used templates with solar metallicity. These adopted SFH are easy to handle but are certainly inappropriate for near-MS star-forming galaxies at these redshifts, where actually the SFRs must have *increased* with time (on average) as a result of the mere existence of the MS (Renzini 2009; Maraston et al. 2010; Peng et al. 2010b; Reddy et al. 2012). As shown by Maraston et al. (2010), for star-forming galaxies, the *age* returned by the SED fit should be interpreted as the typical age of the stars contributing the bulk of the light, rather than the time since the beginning of star formation, as it formally represents in the fits. For this reason, to avoid estimating unrealistic low ages for such galaxies, in which the youngest stellar population outshines the older one, we imposed a lower age limit of 0.1 Gyr.

The *age* returned by the SED fits has yet a different physical meaning in the case of quenched galaxies, i.e. here assumed to be those for which only upper limits can be placed on SFR(UV+IR). As apparent from Table 2, for many such galaxies the fits give $\tau = 0$, which is to say that a single age, SSP provides the best fit. Correspondingly, the age can be interpreted as representative of the time elapsed since quenching. This is a fair interpretation also for the other cases, in which $\tau \neq 0$ but is $\ll$ age, hence the current SFR is very low in the best-fitting exponentially declining model. In the following, we adopt this interpretation for the ages of quenched galaxies.

The SED fitting results are shown in Table 2 and Fig. 3, where symbols are like in Fig. 2. In the left-hand panel of Fig. 3, we compare the best-fitting stellar masses derived using BC03 models, and Salpeter IMF ($M_{\star SED,BC03}$), with those derived following D04 and D07, as explained in Section 3.1 ($M_{\star D04}$). The two quantities agree well, with an average ratio close to unity ($\langle M_{\star D04}/M_{\star SED,BC03} \rangle = 1.05$) and a 1σ scatter of 0.16 dex. By inspecting the optical/nIR best-fitting SEDs of the AGN hosts, we found that most of them do not seems to suffer significant contamination by the AGN emission. On the contrary, two objects (i.e. #1906, and #6898) show a typical 'IRAC power-law' SED, indicating that the AGN component is swamping the stellar emission (Alonso-Herrero et al. 2006; Donley et al. 2007). Hence, for these two objects, in particular, and also for all the AGN hosts with at least a MIPS detection (11/18), we verified that the adopted stellar masses ($M_{\star D04}$) are consistent, (within $\sim$0.25 dex) with those derived by fitting the optical to far-IR SEDs with a modified version of the MAGPHYS software, which also includes the AGN warm dust component (da Cunha, Charlot & Elbaz 2008; Berta et al. 2013).

While the stellar mass inferred from SED fitting is relatively robust, both for quenched and star-forming galaxies (cf. Maraston et al. 2010), the other SED-fitting derived parameters are affected by the well-known degeneracy between the galaxy *age* and reddening ($A_{V, SED}$), then also affecting the measured SFR(SED). However, if properly combined with multiwavelength data (i.e. IR, radio, X), the SED fitting analysis can provide some insight on the nature of the studied galaxies. For instance, it can help to better constrain the reddening and SFR, for galaxies that are undetected in MIPS, and, in general, for galaxies below the MS. This is visible from the middle and right-hand panels of Fig. 3, where the best-fitting reddening values and SFRs are compared with those derived from the IR and UV-uncorrected luminosities ($A_{V, IR + UV}$ and SFR(IR+UV)). For almost all the MIPS-u galaxies, the fit suggests lower values of $A_{V, SED}$, and SFR(SED), with respect to the A_V(IR+UV) and

SFR(IR+UV) upper limits. This strengthen the interpretation of such galaxies as already quenched, or nearly so. When considering only the PACS-d and MIPS-d galaxies, $A_{V, SED}$ and A_V(IR+UV) are on average in good agreement, with a relative difference of $(A_{V, SED} - A_V$(IR+UV))$/A_V$(IR+UV)) $= -0.09$ and 1σ scatter of $\sim$0.41. Some particular cases (flagged with numbers from 1 to 9) in the right-hand and middle panels of Fig. 3 are discussed in Section 4.3.1.

4.3 Observed and rest-frame two-colour plots

In Fig. 4, we explore the observed and rest-frame colours of our sample in two colour–color diagrams widely used in the literature to separate star forming from passive galaxies at high redshifts, i.e. the *BzK* plot (D04) and the rest frame $(U - V)$ versus $(V - J)$ (hereafter *UVJ*) plot (Labbé et al. 2005; Wuyts et al. 2007; Williams et al. 2009). The different sub-samples are colour-coded as labelled in the right-hand panel, and detailed in Section 4.1 and Fig. 2. The *BzK* diagram is a quite efficient criterion to separate galaxies at $1.4 \leq z \leq 2.5$ from those at lower-redshift and among these high-*z* galaxies it separates the star-forming ones (*sBzK*, to be found in the left part of the diagram) from the passive ones (*pBzK*, located within the wedge in the top-right side of the plot). Lower *z* systems are to be found in its bottom-right region of the plot. Rightward arrows in the *BzK* diagram indicate lower limits to the $B - z$ colour, for objects undetected in *B* band. These very red objects include both quenched galaxies (that would be classified as *pBzK*s with deeper *B*-band data) and highly reddened dusty star-forming galaxies (Rodighiero et al. 2014). The *UVJ* diagram (right-hand panel) has the advantage of allowing us to separate dusty star-forming from quenched galaxies at any redshift. In fact, since the dust-free quenched objects have bluer $V - J$ colours with respect to the extincted star-forming galaxies with similarly red $U - V$ colours, they can be isolated on the top-left box of the diagram. We note that galaxies in this region define a tight sequence, which is almost parallel to the diagonal border line of the quenched box. The extent of the 'quenched sequence' mostly depends on the age range spanned by this population, which in our sample is $\sim$0.5–2 Gyr. In fact, young and old quenched objects could be split according to their $V - J$ colour along the sequence (cf. Whitaker et al. 2010). The tightness of the 'quenched sequence' in the *UVJ* plane is instead related to the fact that most of these systems are affected by a small amount of dust reddening. The $U - V$ colour of star-forming galaxies depends on their dust extinction, and separates blue from red dusty objects (cf. Fumagalli et al. 2014).

In the left-hand panel of Fig. 4 some objects do not match the *BzK* criterion, i.e. occupy the lower part of the plot that should contain $z < 1.4$ galaxies (namely, #282, #427, #686, #887, #1187, #1272, #3230, #4705, #5556, #6193, #7491, #7617, and #7923). For some objects (i.e. those closer to the boundaries of the *pBzK* or *sBzK* regions) this could be due to even small photometric errors, and in one case to type-1 AGN contamination (#686). Then, four of the seven MIPS-u galaxies with the bluest $z - K$ colours (i.e. #282, #7491, #7617, and #7923), do not have spectroscopic identification, and could be at slightly lower redshift. However, as shown in fig. 8 of D04, the colours of these objects are also consistent with those of relatively young ($\lesssim$2 Gyr) passively evolving galaxies at $z \sim 1.4-1.5$, characterized by a rapidly declining SFR, which could be missed by a strict *BzK* selection. It is worth noticing that most of these bluer MIPS-u galaxies also lie in the young-quenched region of the *UVJ* diagram, and have SEDs best fitted with SSPs, or declining $\tau = 0.1$ Gyr models with age $\sim$0.7–1.3 Gyr. Hence, we did not exclude any of these sources from the sample.

Table 2. SFR, Stellar Mass, and SED fitting parameters (BC03, models, Salpeter IMF).

ID	SFR(IR+UV) $(M_\odot/yr)$	M_*(D04) $(M_\odot)$	M_*(SED) $(M_\odot)$	Age (Gyr)	A_V (mag)	SFR(SED) $(M_\odot/yr)$	τ (Gyr)	$\tau_{min} - \tau_{max}$ (Gyr)
282	<12.89	11.18	$11.17^{+0.01}_{-0.02}$	$2.10^{+0.00}_{-0.10}$	$0.10^{+0.05}_{-0.05}$	$0.62^{+0.22}_{-0.03}$	0.3	0.3−0.3
427	<12.95	11.26	$11.11^{+0.02}_{-0.01}$	$0.72^{+0.47}_{-0.00}$	$0.50^{+0.05}_{-0.19}$	$1.25^{+0.07}_{-0.02}$	0.1	0.1−0.1
428[a]	<26.31	11.04	$11.11^{+0.03}_{-0.01}$	$3.50^{+0.00}_{-0.01}$	$0.95^{+0.05}_{-0.04}$	$5.58^{+0.32}_{-0.21}$	1.0	1.0−1.0
552	56.23 ± 5.09	11.17	$11.15^{+0.16}_{-0.01}$	$0.72^{+1.18}_{-0.08}$	$1.20^{+0.15}_{-0.20}$	$59.99^{+20.61}_{-12.36}$	0.3	0.3−1.0
557	18.08 ± 4.89	11.01	$11.18^{+0.02}_{-0.01}$	$1.61^{+0.07}_{-0.11}$	$0.50^{+0.05}_{-0.05}$	$3.19^{+0.13}_{-0.62}$	0.3	0.3−0.3
686	332.14 ± 9.39	11.04	$11.04^{+0.01}_{-0.00}$	$0.45^{+0.00}_{-0.01}$	$0.00^{+0.03}_{-0.00}$	$0.00^{+0.00}_{-0.00}$	0.0	0.0−0.0
687	<47.23	11.30	$11.34^{+0.02}_{-0.01}$	$2.10^{+0.10}_{-0.08}$	$0.30^{+0.05}_{-0.05}$	$0.90^{+0.04}_{-0.24}$	0.3	0.3−0.3
720	132.89 ± 6.46	11.06	$11.08^{+0.05}_{-0.01}$	$0.64^{+0.57}_{-0.00}$	$0.60^{+0.01}_{-0.30}$	$2.53^{+0.36}_{-0.03}$	0.1	0.1−0.2
848	<14.65	11.18	$11.11^{+0.04}_{-0.03}$	$1.28^{+0.16}_{-0.00}$	$0.40^{+0.05}_{-0.05}$	$0.00^{+0.00}_{-0.00}$	0.0	0.0−0.1
856	15.09 ± 4.90	11.57	$11.52^{+0.01}_{-0.00}$	$1.28^{+0.00}_{-0.01}$	$0.00^{+0.02}_{-0.00}$	$0.00^{+0.00}_{-0.00}$	0.0	0.0−0.0
880	<32.88	11.23	$11.21^{+0.02}_{-0.01}$	$1.14^{+0.00}_{-0.00}$	$1.65^{+0.05}_{-0.04}$	$16.06^{+0.64}_{-0.50}$	0.3	0.3−0.3
887	<13.94	11.23	$11.05^{+0.02}_{-0.01}$	$1.28^{+0.00}_{-0.00}$	$0.10^{+0.05}_{-0.02}$	$0.00^{+0.00}_{-0.00}$	0.0	0.0−0.0
903	164.43 ± 36.70	11.08	$11.06^{+0.05}_{-0.03}$	$0.18^{+0.11}_{-0.02}$	$2.75^{+0.05}_{-0.05}$	$269.90^{+92.28}_{-44.11}$	0.1	0.1−0.3
947	<15.44	11.06	$11.10^{+0.01}_{-0.02}$	$1.90^{+0.10}_{-0.10}$	$0.30^{+0.05}_{-0.10}$	$1.00^{+0.35}_{-0.30}$	0.3	0.3−0.3
986	<14.65	11.42	$11.33^{+0.01}_{-0.02}$	$1.28^{+0.00}_{-0.00}$	$0.35^{+0.03}_{-0.05}$	$0.00^{+0.00}_{-0.00}$	0.0	0.0−0.0
1084	<9.58	11.21	$11.22^{+0.02}_{-0.01}$	$2.10^{+0.10}_{-0.10}$	$0.15^{+0.10}_{-0.05}$	$0.69^{+0.30}_{-0.19}$	0.3	0.3−0.3
1187	<14.38	11.24	$11.26^{+0.01}_{-0.01}$	$1.61^{+0.04}_{-0.00}$	$0.45^{+0.02}_{-0.06}$	$3.80^{+0.09}_{-0.54}$	0.3	0.3−0.3
1272	<18.00	11.06	$10.91^{+0.01}_{-0.02}$	$1.28^{+0.00}_{-0.00}$	$0.40^{+0.04}_{-0.05}$	$0.00^{+0.00}_{-0.00}$	0.0	0.0−0.0
1510	238.82 ± 13.20	11.08	$11.01^{+0.02}_{-0.04}$	$0.23^{+0.03}_{-0.02}$	$1.90^{+0.05}_{-0.10}$	$141.22^{+27.38}_{-31.95}$	0.1	0.1−0.1
1906	123.32 ± 24.14	11.04	$10.74^{+0.01}_{-0.00}$	$0.10^{+0.00}_{-0.00}$	$1.65^{+0.02}_{-0.00}$	$621.53^{+19.18}_{-15.98}$	1000.0	1.0−1000
2450	<10.44	11.02	$11.14^{+0.01}_{-0.02}$	$1.61^{+0.09}_{-0.00}$	$0.55^{+0.02}_{-0.10}$	$2.87^{+0.06}_{-0.75}$	0.3	0.3−0.3
2470	133.70 ± 43.62	11.02	$11.31^{+0.04}_{-0.36}$	$3.50^{+0.25}_{-3.27}$	$2.25^{+0.80}_{-0.20}$	$41.31^{+81.14}_{-14.64}$	3.0	0.1−1000
2940	<12.10	11.22	$11.30^{+0.04}_{-0.02}$	$1.28^{+0.03}_{-0.14}$	$0.60^{+0.25}_{-0.04}$	$12.67^{+9.25}_{-0.43}$	0.3	0.3−0.3
3066	93.05 ± 27.05	11.12	$10.84^{+0.02}_{-0.02}$	$0.10^{+0.01}_{-0.00}$	$3.00^{+0.00}_{-0.05}$	$770.96^{+14.06}_{-105.34}$	1000.0	0.3−1000
3230	<32.67	11.09	$11.00^{+0.02}_{-0.02}$	$1.28^{+0.00}_{-0.00}$	$0.15^{+0.05}_{-0.05}$	$0.00^{+0.00}_{-0.00}$	0.0	0.0−0.0
3231	<37.14	11.65	$11.68^{+0.02}_{-0.01}$	$1.90^{+0.06}_{-0.00}$	$0.55^{+0.05}_{-0.06}$	$3.80^{+0.19}_{-0.67}$	0.3	0.3−0.3
3236	114.20 ± 16.96	11.03	$10.98^{+0.01}_{-0.04}$	$0.20^{+0.01}_{-0.02}$	$1.70^{+0.10}_{-0.02}$	$176.47^{+45.19}_{10.98}$	0.1	0.1−0.1
3258	<14.91	11.31	$11.38^{+0.01}_{-0.02}$	$2.00^{+0.10}_{-0.10}$	$0.35^{+0.05}_{-0.05}$	$1.38^{+0.49}_{-0.41}$	0.3	0.0−0.3
3853	23.44 ± 6.11	11.31	$11.30^{+0.01}_{-0.02}$	$1.14^{+0.00}_{-0.04}$	$1.05^{+0.07}_{-0.05}$	$20.14^{+4.05}_{-1.09}$	0.3	0.3−0.3
4310	<10.49	11.03	$10.95^{+0.02}_{-0.02}$	$1.28^{+0.00}_{-0.00}$	$0.40^{+0.05}_{-0.05}$	$0.00^{+0.00}_{-0.00}$	0.0	0.0−0.0
4406	137.21 ± 63.97	11.21	$11.24^{+0.02}_{-0.01}$	$1.14^{+1.31}_{-0.00}$	$2.55^{+0.10}_{-0.05}$	$17.38^{+0.77}_{-0.39}$	0.3	0.3−0.3
4705	199.93 ± 5.83	11.01	$10.91^{+0.03}_{-0.03}$	$0.23^{+0.03}_{-0.02}$	$2.80^{+0.10}_{-0.05}$	$112.53^{+30.33}_{23.24}$	0.1	0.1−0.1
5149	<12.22	11.10	$11.14^{+0.00}_{-0.02}$	$1.80^{+0.07}_{-0.12}$	$0.40^{+0.10}_{-0.05}$	$1.55^{+0.72}_{-0.06}$	0.3	0.3−0.3
5415	39.38 ± 5.00	11.05	$11.12^{+0.00}_{-0.03}$	$0.81^{+0.05}_{-0.09}$	$1.00^{+0.10}_{-0.08}$	$40.98^{+11.56}_{-5.79}$	0.3	0.3−0.3
5503	426.87 ± 9.27	11.06	$10.95^{+0.05}_{-0.02}$	$0.18^{+0.00}_{-0.01}$	$1.80^{+0.03}_{-0.15}$	$211.19^{+23.34}_{72.04}$	0.1	0.1−0.1
5509	<13.54	11.32	$11.54^{+0.03}_{-0.01}$	$3.75^{+0.00}_{-0.25}$	$1.85^{+0.10}_{-0.05}$	$11.46^{+2.99}_{-0.34}$	1.0	1.0−1.0
5530	<27.52	11.10	$10.94^{+0.01}_{-0.01}$	$1.70^{+0.10}_{-0.10}$	$0.30^{+0.05}_{-0.10}$	$1.35^{+0.13}_{-0.38}$	0.3	0.3−0.3
5534	375.88 ± 10.78	11.23	$11.23^{+0.02}_{-0.01}$	$0.32^{+0.00}_{-0.03}$	$2.45^{+0.15}_{-0.03}$	$88.29^{+39.43}_{-2.15}$	0.1	0.1−0.1
5556	<24.83	11.08	$11.03^{+0.02}_{-0.01}$	$0.81^{+0.00}_{-0.00}$	$0.45^{+0.04}_{-0.03}$	$0.43^{+0.02}_{-0.01}$	0.1	0.1−0.1
5564	<9.34	11.22	$11.34^{+0.01}_{-0.02}$	$2.00^{+0.10}_{-0.07}$	$0.30^{+0.07}_{-0.10}$	$1.27^{+0.38}_{-0.38}$	0.3	0.3−0.3
5860	141.95 ± 15.23	11.40	$11.33^{+0.02}_{-0.01}$	$0.29^{+0.00}_{-0.03}$	$2.45^{+0.15}_{-0.06}$	$158.60^{+64.16}_{-27.17}$	0.1	0.1−0.1
5974	511.86 ± 24.04	11.01	$11.20^{+0.03}_{-0.09}$	$0.64^{+0.08}_{-0.35}$	$2.20^{+0.25}_{-0.10}$	$90.06^{+22.89}_{-21.08}$	0.3	0.1−0.3
6071	185.39 ± 37.17	11.29	$11.10^{+0.05}_{-0.06}$	$0.20^{+0.12}_{-0.07}$	$2.85^{+0.05}_{-0.05}$	$513.46^{+141.29}_{-138.94}$	0.3	0.1−1000
6193	126.22 ± 8.65	11.32	$11.19^{+0.00}_{-0.00}$	$0.64^{+0.00}_{-0.01}$	$0.60^{+0.00}_{-0.01}$	$3.28^{+0.00}_{-0.02}$	0.1	0.1−0.1
6224	74.75 ± 11.88	11.02	$10.68^{+0.06}_{-0.07}$	$0.20^{+0.08}_{-0.06}$	$2.35^{+0.05}_{-0.10}$	$280.64^{+42.58}_{-60.14}$	1000.0	0.3−1000
6352	91.69 ± 21.73	11.03	$10.94^{+0.03}_{-0.00}$	$0.32^{+0.04}_{-0.03}$	$1.15^{+0.15}_{-0.09}$	$45.71^{+20.56}_{-12.08}$	0.1	0.1−0.1
6572	265.86 ± 77.08	11.08	$11.50^{+0.05}_{-0.09}$	$3.00^{+0.00}_{-1.20}$	$2.00^{+0.15}_{-0.20}$	$132.45^{+43.37}_{-44.91}$	30.0	3.0−1000
6647	<20.92	11.10	$11.14^{+0.01}_{-0.02}$	$1.28^{+0.04}_{-0.00}$	$0.60^{+0.00}_{-0.05}$	$0.00^{+0.00}_{-0.00}$	0.0	0.0−0.0
6898	90.28 ± 16.12	11.41	$11.56^{+0.05}_{-0.09}$	$1.43^{+0.47}_{-0.79}$	$2.25^{+0.20}_{-0.15}$	$305.12^{+138.28}_{-78.62}$	10.0	1.0−1000
7077	83.23 ± 6.59	11.22	$11.17^{+0.02}_{-0.00}$	$0.36^{+0.00}_{-0.04}$	$1.65^{+0.15}_{-0.01}$	$51.81^{+25.23}_{-0.54}$	0.1	0.1−0.1

Table 2 – *continued*

ID	SFR(IR+UV) ($M_\odot/yr$)	M_*(D04) ($M_\odot$)	M_*(SED) ($M_\odot$)	Age (Gyr)	A_V (mag)	SFR(SED) ($M_\odot/yr$)	τ (Gyr)	$\tau_{min} - \tau_{max}$ (Gyr)
7116	90.94 ± 31.19	11.13	$11.29^{+0.01}_{-0.04}$	$4.00^{+0.00}_{-0.75}$	$1.75^{+0.05}_{-0.10}$	$66.21^{+6.91}_{-10.96}$	1000.0	$10.0-1000$
7491	<9.68	11.09	$10.98^{+0.01}_{-0.02}$	$1.28^{+0.00}_{-0.00}$	$0.15^{+0.03}_{-0.05}$	$0.00^{+0.00}_{-0.00}$	0.0	$0.0-0.0$
7617	<14.47	11.03	$10.97^{+0.03}_{-0.03}$	$1.28^{+0.23}_{-0.00}$	$0.00^{+0.00}_{-0.00}$	$0.00^{+0.00}_{-0.00}$	0.0	$0.0-0.0$
7923	<11.91	11.11	$11.01^{+0.00}_{-0.02}$	$1.90^{+0.01}_{-0.10}$	$0.00^{+0.05}_{-0.00}$	$0.83^{+0.28}_{-0.11}$	0.3	$0.3-0.3$
8121	<10.25	11.37	$11.51^{+0.02}_{-0.01}$	$1.90^{+0.10}_{-0.03}$	$0.25^{+0.04}_{-0.10}$	$2.62^{+0.12}_{-0.76}$	0.3	$0.3-0.3$
8569	140.69 ± 9.35	11.33	$11.14^{+0.01}_{-0.01}$	$0.23^{+0.03}_{-0.01}$	$1.75^{+0.02}_{-0.10}$	$191.17^{+14.01}_{-44.35}$	0.1	$0.1-0.1$

Note. [a]Lens galaxy candidate. We show here the SED best-fit parameters derived by masking out the ring in each filter, as detailed in Section 5.3. By using the original photometry from the D07 catalog (without masking the ring) we obtained the following results: M_*(SED) $= 10.99^{+0.03}_{-0.01}$, Age $= 3.75^{+0.25}_{-1.55}$, $A_V = 1.10^{+0.15}_{-0.15}$, SFR(SED) $= 33.11^{+10.82}_{-8.33}$, $\tau = 30.0$, $[\tau_{min} - \tau_{max}] = [3.0 - 1000]$.

The second column shows the total SFR(IR+UV), where the IR contribution is derived from the IR SEDs, 24 μm/MIPS flux, or 24 μm/MIPS upper limit, for PACS-d, MIPS-d, and MIPS-u galaxies, respectively, as detailed in Section 3.2. M_*(D04), and M_*(SED) are stellar masses derived as in D04, and from the best-fit SED, respectively. Other best-fit SED quantities follow; in the order: mean stellar-age, reddening (A_V), SFR, declining τ, and τ 90% confidence interval. All the uncertainties on the SED-derived quantities are within the 90% confidence level, and inferred from the χ^2 test. Typical uncertainties on M_*(D04) are around 40% (cf., D04).
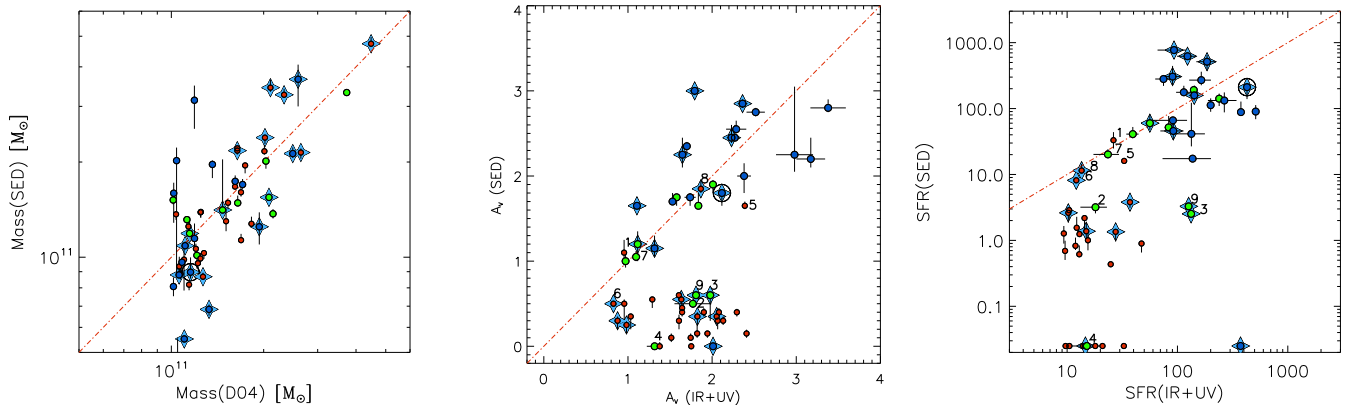
Figure 3. The SED fitting derived Mass, SFR, and reddening are compared with the same quantities, as derived with different methods. In all the panels symbols are like in Fig. 2. The numbers from 1 to 9, labelled in the middle and right-hand panels, represent the odd cases discussed in Section 4.3.1, and correspond to objects: #428=1, #557=2, #720=3, #856=4, #880=5, #2940=6, #3853=7, #5509=8, #6193=9. Left-hand panel: best-fitting masses ($M_{*\rm SED}$) versus masses derived from K-band magnitude (M_{*D04}). Middle panel: best-fitting reddening ($A_{V,\rm SED}$) versus A_V(IR+UV), derived from the ratio between the total and UV uncorrected SFR. Right-hand panel: best-fitting SFR (SFR$_{\rm SED}$) versus SFR(IR+UV), derived as explained in Section 3.2.

In Fig. 4, the galaxy colours strongly correlate with their position relative to the MS: MIPS-u galaxies are generally in the 'quenched regions' (*pBzK*, and *pUVJ*), and PACS-d galaxies in the star-forming regions (*sBzK*, and *sUVJ*), in both the panels. With two exceptions, the MIPS-d objects lie in the star-forming region in the *BzK* diagram, while half of them are in the quenched region in the *UVJ* diagram. In the next section, we will discuss these objects, together with other peculiar cases.

4.3.1 A few odd cases

A few objects show *BzK* or *UVJ* colours and best-fitting SED which are apparently at odd with respect to their position relative to the MS. In some cases this is due to (even small) photometric errors, but in other cases this could indicate a different nature of these 'outliers' (i.e. star-forming galaxies with a relatively old age, on the way to be quenched, or rejuvenated, AGN, etc.), as discussed below. To facilitate the identification of these objects in Figs 3 and 4, we flagged them with numbers from 1 to 9.

Object #428 ('1' in the figures) is a MIPS-u galaxy, but shows colours similar to star-forming galaxies, i.e. lies in the *sBzK* and *sUVJ* regions. Judging from its appearance (see Fig. 9), this object may be a lens ETG surrounded by a blue arc. So, the blue colours can be due to the magnified background source when the photometry does not separate the arc from the central galaxy. Indeed, the rest-frame colours of the central galaxy, having masked out the blue arc as detailed in Section 5.2, are $(U - V) = 1.93$ and $(V - J) = 1.58$, consistent with those of a quenched object (see Section 5.3).

There are two MIPS-u objects in the dusty-star-forming box of the *UVJ* plane. They are #880, and #5509 (flagged as '5', and '8'), and in the *BzK* diagram are shown as lower limit to $B - z$, being undetected in B band. Their *BzK* colours are compatible with those of old red galaxies, but the SED fitting analysis indicates a higher reddening and SFR(SED) with respect to other MIPS-u objects (cf. Fig. 3 and Table 2), yet still in agreement with the upper limits derived from the 24 μm/MIPS. In particular, since object #880 is one of the MIPS-deblended sources (see Section 2.1 and Appendix A), we do not exclude that it has a low residual star formation (partly
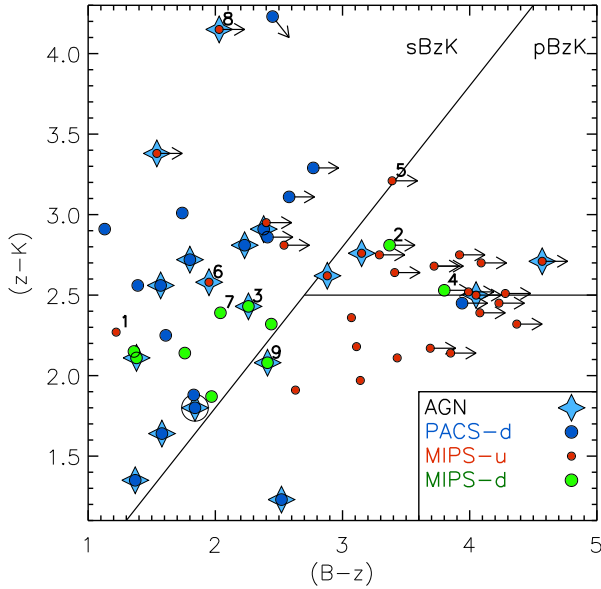
Figure 4. BzK and UVJ diagrams for the three sub-samples, where MIPS-u are the red filled circles, MIPS-d are green filled circles and PACS-d are blue filled circles, as labelled in the right-hand panel of the figure. X-ray sources and IRAC power-law are also highlighted by cyan stars. The odd cases discussed in Section 4.3.1 are flagged with numbers from 1 to 9, as in Fig. 3.

contributing to the MIPS blended source). However, it is also very close to the boundaries of the *pUVJ* region, and, alternatively, its odd position in the *UVJ* colour diagram could just depend on small photometric errors. The AGN host #5509 is undetected, or very faint, in all the optical bands. Its location in the dusty-*sUVJ* could be due to residual obscured star formation, which could also be responsible of the marginal 24 μm/MIPS detection of the object (2.5σ, see Section 4, and Table 1). It is also possible that the AGN partly, or totally, contributes to the low MIPS emission of the source, and that its odd position on the *UVJ* diagram is instead due to a higher redshift with respect to the photo-*z* quoted here (Grazian et al. 2006, for instance, Luo et al. 2010 and Hsu et al. 2014 report $z_{\rm phot} \simeq 2.5$).

Object #2940 (flagged as '6') is a MIPS-u AGN host lying in the *sBzK* region. It is in the quenched region of the *UVJ* diagram, but its bluer $B - z$ colour could indicate that a low residual star formation is still present. The SFR inferred from the best-fitting SED is ∼8 M⊙ yr⁻¹, which is very close to the upper limit from MIPS (cf. the right-hand panel of Fig. 3).

Two of the MIPS-d galaxies >4 times below the MS, i.e. #557 and #856 (labelled as '2', and '4', respectively) lie in the quenched region, both in the *BzK*, and in the *UVJ* diagram. Moreover, their best-fitting SEDs indicate a very low SFR (i.e. SFR(SED) < 3 M⊙ yr⁻¹), and modest extinction (cf. Table 2 and Fig. 3). Hence, they are likely to be quenched galaxies, where the 24 μm/MIPS detection (slightly above 3σ) could be due to old AGB stars, or alternatively to a highly obscured AGN, rather than to star formation. In the following, we consider them as quenched galaxies.

On the other hand, the third MIPS-d galaxy below the MS, #3853 (labelled as '7'), seems to have a different nature with respect to the other two discussed above. It also lies in the quenched region of the *UVJ* diagram, and has a red, $z - K$ colour ($\simeq 2.4$), consistent with a relatively old age (1.14 Gyr, cf. Table 2), but it is classified as an *sBzK*, due to the bluer $B - z$ colour. This seems to indicate that the 24 μm/MIPS emission is plausibly powered by a low residual star formation, as also confirmed by the SED fitting results in Fig. 3 (A_V(SED) = 0.99, and SFR(SED)=20 M⊙ yr⁻¹, in agreement with that derived from MIPS, SFR(IR+UV)=23 ± 6M⊙ yr⁻¹).
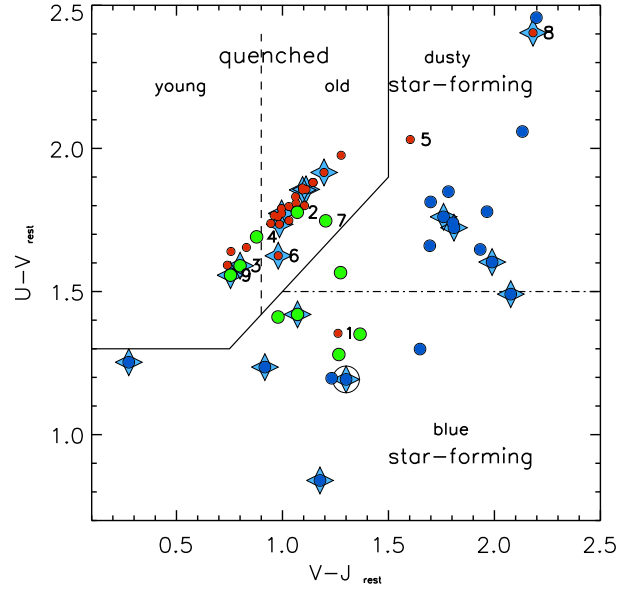
The MIPS-d AGN objects #720 and #6193 (i.e. '3' and '9') have observed colours typical of *sBzK* but lie in the 'young-quenched' region of the *UVJ* diagram. In fact, they are redder with respect to the other MIPS-d galaxies *on the* MS, and best fit with declining SFR with $\tau = 0.1$ stellar population models, age = 0.64 Gyr, low reddening, and SFR(SED) ∼ 2–3 M⊙ yr⁻¹. These results do not agree with the high SFR(IR+UV) > 100 M⊙ yr⁻¹ and large reddening (∼1.8–2 mag) derived from the 24 μm/MIPS emission of these galaxies. If the AGNs were responsible of most of the MIPS emission, both of these objects should be shifted below the MS in Fig. 2, entering the sub-sample of quenched galaxies. However, it is not trivial to estimate the fraction of the IR luminosity due to the AGN and to obscured star formation, because both objects are undetected in the far-IR. The bluer observed colours, and the younger best-fitting *age* of these galaxies, with respect to other MIPS-u quenched galaxies in the sample (including AGN hosts), seems to suggest that they are still star forming, but maybe on the way to be quenched (possibly triggered by the AGN). On the contrary, the third AGN among the MIPS-d galaxies, i.e. #552, shows *BzK/UVJ* colours and best-fitting SED consistent with a moderate unobscured star-formation activity, in agreement with what expected based on the MIPS emission (SFR_SED ≈ SFR(IR+UV) ≈ 56 M⊙ yr⁻¹).

4.3.2 Summary of the source classification

As shown in the previous sections, for galaxies lying more than 4 times below the MS the best-fitting SEDs provide stricter upper limits to their SFR, compared to the limits set by the 24 μm/MIPS data. Hence, hereafter we use these new upper limits to the SFR for all the MIPS-u galaxies, as well as for the three MIPS-d galaxies located below the MS (i.e. #557, #856, and #3853, flagged as '2', '4', and '7' in Figs 3 and 4).

Fig. 5, shows the distribution of the sources as a function of the 'distance' from the MS, parametrized as the sSFR normalized to that predicted by equation (1) for an MS galaxy of the same mass, in logarithmic scale, i.e. log(sSFR/sSFR_MS)). The red solid and dot–dashed lines in the figure show the average MS, and the
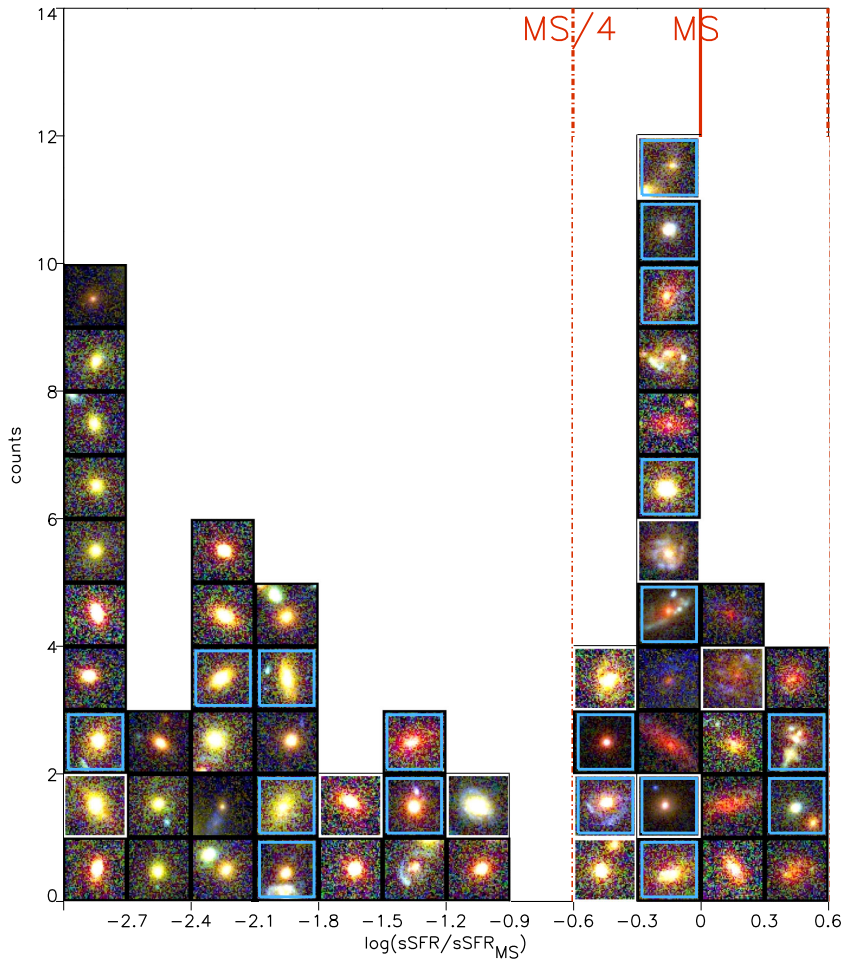
Figure 5. The distribution of the sample galaxies as a function of the 'distance' from the MS, i.e. the $\log(sSFR/sSFR_{MS})$. As explained in the text, hereafter, we used the SFR inferred from the best-fitting SED (SFR(SED)) for all the galaxies below the MS strip. Within each $\log(sSFR/sSFR_{MS})$ bin the distance from the MS also increases from top to bottom. On the contrary, in the first bin, which only includes galaxies best fitted with an SSP, and with SFR(SED) = 0, objects are ordered randomly. The red solid and dot–dashed lines show the MS, and the loci four times above and below it, respectively. The MIPS-detected (and PACS-undetected) galaxies are distinguished by the white frames, and AGN hosts by a cyan frame. The postage stamps are red–green–blue (R-G-B) composite images (R = *F160W*, G = *F850LP*, B = *F435W*) of 3 arcsec size.

offsets of ±0.6 dex, corresponding to four times above, and below it. The MIPS-d galaxies (undetected in the FIR, hence which are not PACS-d galaxies) are highlighted with a white frame. Within the MS band all other galaxies are detected in the FIR, while outside this band none of the galaxies is detected. AGN hosts are identified by a cyan frame. The first $\log(sSFR/sSFR_{MS})$ bin of the histogram includes only galaxies which are best fitted by an SSP, hence with SFR(SED) = 0. For each of the remaining bins, the postage stamps are displayed in such a way that the distance from the MS also increases, i.e. $\log(sSFR/sSFR_{MS})$ decreases, from top to bottom along the *y* axis.

Out of the 56 most massive galaxies at $1.4 \leq z \leq 2$ in GOODS-S, 25 objects (~45 per cent) are on the MS, i.e. within a factor of 4 (±0.6 dex in Fig. 5) from the average MS relation at $z \simeq 1.7$, while 31 objects (~55 per cent) are below it ($\log(sSFR/sSFR_{MS}) < -0.6$). Several authors have found a *flattening* of the MS slope at the high-mass end (e.g. Bauer et al. 2011; Wuyts et al. 2011; Whitaker et al. 2012; Rodighiero et al. 2014), interpreted as a further evidence that the mass-quenching process is more efficient on the most massive galaxies (Peng et al. 2010b). Also here the fraction of MS galaxies below the average relation (2/3) exceeds the fraction above it (1/3),

although the sample is too small to establish the significance of this result. On the other hand, if the transition from star forming to passive galaxies is linked to a morphological transformation, one cannot exclude that the appearance of passive bulges in the most evolved massive star-forming galaxies, contributing to the galaxy M_* but not much to its SFR could flatten the MS slope at the highest masses (Bruce et al. 2014; Lang et al. 2014, and Tacchella et al. 2014a). Actually, a visual inspection of the image stamps in Fig. 5, seems to confirm that many MS galaxies with $-0.6 < \log(sSFR/sSFR_{MS}) < 0$ host a bulge. As shown in the following, this has been also confirmed through a 2D SB fitting in the *HST*/WFC3 images (Section 5).

At the end of this exercise, i.e. after the deblending procedure, and the use of SED fitting to better constrain the SFR for galaxies below the MS, we conclude that all the galaxies below the MS band have an sSFR more than 10 times lower than that of MS galaxies in the same redshift range, and most of them ~100–1000 times lower (Fig. 5). Their global properties are also typical of quenched objects. This suggests that at $z \sim 1.4$–2 the mass quenching may be a relatively fast process, much shorter than the time spent by these galaxies in their massive phase within the MS band (i.e. a transition

time $\ll \sim 1$ Gyr), as one may expect if quenching is caused by the sudden expulsion of all the gas and dust from the galaxy.

In summary, our sample of 56 galaxies splits in two main groups: (i) the *MS galaxies*, included in the MS band ($-0.6 <$ log(sSFR/sSFR$_{MS}$) < 0), and (ii) the *quenched galaxies*, with log(sSFR/sSFR$_{MS}$) < -1, which have a mass doubling time (the time needed by the galaxy to double its M_*, in case it continues to form stars at the present rate) ≥ 10 Gyr. In our small sample a well defined, sizeable class of objects *on the way to be quenched* cannot be unambiguously recognized. Such transition galaxies could be found among the *MS galaxies* with the lowest sSFR ($-0.6 <$ log(sSFR/sSFR$_{MS}$) < 0), and/or among the *quenched galaxies* with the highest sSFR upper limits ($-2 \lesssim$ log(sSFR/sSFR$_{MS}$) $\lesssim -0.6$). Clearly a much bigger sample should be analysed to adequately populate this class of objects which must exist and should allow us to estimate the *quenching time-scale*. However, the present investigation demonstrates that a careful, object-by-object study is necessary to identify bona fide transition objects, given that blending may lead to gross errors in the estimated SFRs, especially for this class of galaxies (see Fig. 2).

5 MORPHOLOGICAL CLASSIFICATION

5.1 Single-Sérsic SB fitting

We used GALFIT to fit the SB profile of our galaxies. Since the sample includes both star-forming and quenched high-z massive galaxies, for a first analysis we fit the SB profiles of each galaxy in the *F160W*/WFC3 filter (H band) with a single-Sérsic function (Sersic 1968), leaving the Sérsic index (n) as a free parameter. In general, the SB distribution of high-z galaxies is far from following a regular Sérsic profile, and especially so those of star-forming galaxies, that often are clumpy or merger-like systems (Epinat et al. 2009; Förster Schreiber et al. 2009; Genzel et al. 2011). However, this method allows us to classify objects as either ETG(bulge-dominated, $n > 2$–2.5) or late-type galaxies (disc-dominated, $n < 2$–2.5). Three out of the 56 galaxies have irregular morphology, and show strong residuals when fitted with a single-Sérsic profile, or with a bulge+disc model. They are the AGN 'candidate' #5503 (see Section 3.3), and the inactive galaxies #3236, and #5534, which have been excluded from the morphological analysis presented in the following. To reliably measure the sky background, we run GALFIT on large images, of 30 arcsec in size centred on each galaxy, and fit together all the brightest sources ($H < 23.5$) included in the field (masking out the fainter ones). A prior run with SEXTRACTOR (Bertin & Arnouts 1996) on the same images provided the morphological parameters to be set as starting point in the fit. The PSF model was built using the 10–20 closest unsaturated stars in the field. All the parameters, i.e. sky background, Sérsic index (n), centroid, total magnitude (m_{160}), half-light semi-major axis (a_e), position angle (PA), and axial ratio (b/a), were left as free. The results are reported in Table 3 and Fig. 6.

The left-hand panel of Fig. 6 shows the index n as a function of the distance from the MS at $\langle z \rangle = 1.7$, i.e. log(sSFR/sSFR$_{MS}$). The PACS-d, MIPS-d, and MIPS-u sub-samples are shown in blue, green, and red, respectively, and the AGN highlighted with cyan four-point stars, such as in Figs 2–4. The vertical solid, and dash-dotted lines represent the MS (equation 2), and its four times lower boundary (labelled as 'MS/4'), respectively. The Sérsic $n = 2.5$ line shows the separation between 'Early-Type' (or bulge-dominated) and 'Late-Type' (or disc-dominated) galaxies. The right-hand panel

of the same figure, shows the distance from the MS versus the distance from the M_*–R_e relation of local ETGs (i.e. the circularized effective radius, R_e, normalized to the value at $z = 0$, R$_0$, from Shen et al. 2003). Here, we use the M_*–R_e relation of local ETGs as a reference for both the quenched and the star-forming galaxies in our sample, as $z \sim 1.4$–2 star-forming galaxies with such high masses (and SFRs) will necessarily be quenched in a relatively short time (to avoid mass overgrowing), and then passively evolve down to $z = 0$ without major further increase in mass. The bottom panels show the mean values of the same quantities, in log(sSFR/sSFR$_{MS}$) bins chosen so to have 7–11 objects per bin. Black filled circles are relative to all the objects within a bin, while red open squares are obtained by only considering galaxies without evidence of AGN.

From Fig. 6, it appears that almost all the *quenched galaxies* show an 'early-type' morphology, with $n > 2$–2.5, and a circularized effective radius (R_e) from 1.4 to 5 (2.5 on average) times smaller with respect to the local ETGs of the same mass, a well-known property of high-z quenched galaxies. On the contrary, *MS galaxies* split in two groups, above and below the border-line at $n = 2.5$. Almost all the MS galaxies with $n > 2$–2.5 host an AGN, whereas all the AGN host have $n > 2$ (but the AGN 'candidate', #5503, which has irregular morphology and is not shown in the figure). The high Sérsic index of the AGN hosts could be due either to the nuclear emission of the AGN itself, detected as a central, unresolved point-source, or to a significant bulge component (cf. Rosario et al. 2015). We investigate this issue in Section 5.2, by means of SB profile decomposition, in bulge+disc, and bulge+disc+PSF components.

MS galaxies have in general size comparable with those of local ETGs, a part from four AGN hosts (i.e. #1906, #6898, #6193, #6352), and one normal galaxy (#5415), which are comparable to the compact star-forming galaxies (CSFGs) identified by Barro et al. (2013, 2014, hereafter B13 and B14) at $1.4 < z < 3$, and considered the direct progenitors of compact quenched systems at similar redshifts. Since, as mentioned in Section 4.2, #1906, and #6898 are contaminated by the AGN in their photometric SEDs, it is not clear if their compact size are intrinsical, or just due to the AGN affecting the SB profile (cf. also the discussion in Section 5.2). In any case, all these five objects have a relatively low sSFR, lying in the region $-0.6 <$ log(sSFR/sSFR$_{MS}$) < 0 of Fig. 6, consistently with having started their quenching phase.

Concerning the quenched population, our results are in agreement with the well-documented smaller size of the high-z quenched galaxies with respect to the local ones (e.g. Daddi et al. 2005; Trujillo et al. 2006, 2007; Longhetti et al. 2007; Toft et al. 2007; Buitrago et al. 2008; Cimatti et al. 2008; McGrath et al. 2008; van Dokkum et al. 2008; Damjanov et al. 2009; Saracco, Longhetti & Andreon 2009; Cassata et al. 2010; B13; Bezanson et al. 2013; Szomoru et al. 2013). On the other hand, not all the quenched galaxies at high-z have been found to be undersized, both in the field and in protoclusters (Mancini et al. 2010; Saracco, Longhetti & Gargiulo 2011; Stott et al. 2011; Onodera et al. 2012; Huertas-Company et al. 2013). It has been suggested that the average size growth of ETGs from $z = 3$ to 0 is not (or not only) due to the evolution of the individual galaxies (e.g. by mergers), but mostly (or partly) caused by the gradual addition of larger, newly quenched galaxies at lower redshifts (Valentinuzzi et al. 2010; Carollo et al. 2013; Cassata et al. 2013; Poggianti et al. 2013), although some authors have a different view (e.g. van der Wel et al. 2009). In our sample, the scarcity of compact with respect to normal star-forming galaxies, could be interpreted as an indication that the majority of the incoming quenched galaxies at $z \lesssim 1.4$ are progressively larger

Table 3. Morphological parameters from the GALFIT 2D SB fitting on the WFC3/f160W (*H*-band) images.

ID	mag (AB)	n	$R_{e, circ}$ (kpc)	B/T	PSF/T (sS+PSF)	$\log \frac{sSFR}{sSFR(MS)}$	$\frac{R_{e, circ}}{R_0}$
282	21.31 ± 0.01	4.68 ± 0.08	1.63 ± 0.02	0.83 ± 0.01	<0.1	$-2.45^{+0.16}_{-0.02}$	0.41
427	20.91 ± 0.01	3.73 ± 0.04	2.4 ± 0.02	0.47 ± 0.02	0.15 ± 0.006	$-2.20^{+0.02}_{-0.01}$	0.55
428[a]	21.96 ± 0.02	3.65 ± 0.08	3.90 ± 0.05	0.33 ± 0.01	<0.1	$-1.38^{+0.02}_{-0.02}$	1.20
552	21.18 ± 0.01	4.01 ± 0.09	3.66 ± 0.08	0.54 ± 0.04	<0.1	$-0.47^{+0.04}_{-0.04}$	0.95
557	22.28 ± 0.01	2.26 ± 0.04	2.07 ± 0.02	0.65 ± 0.03	<0.1	$-1.59^{+0.02}_{-0.08}$	0.66
686	21.73 ± 0.02	4.02 ± 0.19	2.55 ± 0.05	0.85 ± 0.04	0.22 ± 0.01	$0.45^{+0.03}_{-0.03}$	0.78
687	21.37 ± 0.01	2.66 ± 0.02	1.8 ± 0.0	0.62 ± 0.02	<0.1	$-2.38^{+0.02}_{-0.12}$	0.39
720	21.72 ± 0.09	3.39 ± 0.42	4.71 ± 0.73	0.32 ± 0.05	<0.1	$-0.01^{+0.02}_{-0.02}$	1.41
848	21.58 ± 0.01	3.23 ± 0.05	0.88 ± 0.01	0.83 ± 0.02	<0.1	<-3.0	0.23
856	20.45 ± 0.01	5.31 ± 0.04	2.85 ± 0.02	0.86 ± 0.02	0.10 ± 0.01	<-3.0	0.44
880	21.91 ± 0.01	4.8 ± 0.16	1.59 ± 0.03	1.0 ± 0.0	<0.1	$-1.06^{+0.02}_{-0.01}$	0.38
887	21.04 ± 0.01	5.9 ± 0.08	2.38 ± 0.03	0.76 ± 0.02	<0.1	<-3.0	0.57
903	22.18 ± 0.01	0.88 ± 0.01	4.36 ± 0.03	0.0 ± 0.0	<0.1	$0.07^{+0.10}_{-0.10}$	1.28
947	21.83 ± 0.01	2.69 ± 0.05	0.7 ± 0.0	0.71 ± 0.03	<0.1	$-2.13^{+0.15}_{-0.13}$	0.21
986	20.96 ± 0.01	6.27 ± 0.09	1.89 ± 0.02	0.79 ± 0.02	<0.1	<-3.0	0.35
1084	21.63 ± 0.01	2.59 ± 0.04	1.13 ± 0.01	0.0 ± 0.0	0.24 ± 0.01	$-2.41^{+0.19}_{-0.12}$	0.28
1187	21.5 ± 0.01	2.73 ± 0.02	2.11 ± 0.01	0.0 ± 0.0	0.18 ± 0.01	$-1.94^{+0.01}_{-0.14}$	0.50
1272	21.74 ± 0.01	2.54 ± 0.03	2.02 ± 0.02	0.81 ± 0.02	<0.1	<-3.0	0.61
1510	21.61 ± 0.01	1.01 ± 0.01	6.94 ± 0.08	0.0 ± 0.0	0.10 ± 0.05	$0.22^{+0.02}_{-0.02}$	2.02
1906	21.39 ± 0.01	5.01 ± 0.05	1.68 ± 0.01	1.0 ± 0.0	<0.1	$-0.03^{+0.09}_{-0.09}$	0.52
2450	22.12 ± 0.01	1.9 ± 0.03	0.99 ± 0.0	0.49 ± 0.02	<0.1	$-1.64^{+0.01}_{-0.11}$	0.31
2470	22.63 ± 0.01	1.25 ± 0.02	2.58 ± 0.02	0.0 ± 0.0	0.10 ± 0.01	$0.02^{+0.14}_{-0.14}$	0.82
2940	21.26 ± 0.01	5.42 ± 0.09	2.03 ± 0.03	0.89 ± 0.02	0.17 ± 0.01	$-1.35^{+0.01}_{-0.01}$	0.50
3066	21.6 ± 0.01	2.72 ± 0.04	5.11 ± 0.08	0.15 ± 0.01	0.10 ± 0.01	$-0.22^{+0.13}_{-0.13}$	1.41
3230	21.69 ± 0.01	3.41 ± 0.03	1.23 ± 0.01	0.65 ± 0.04	0.14 ± 0.05	<-3.0	0.35
3231	20.42 ± 0.01	2.53 ± 0.01	6.62 ± 0.03	0.63 ± 0.01	<0.1	$-2.02^{+0.02}_{-0.08}$	0.92
3236	—	—	—	—	—	$-0.06^{+0.06}_{-0.06}$	—
3258	21.17 ± 0.01	1.85 ± 0.01	2.01 ± 0.01	0.38 ± 0.02	<0.1	$-2.19^{+0.15}_{-0.13}$	0.44
3853	21.06 ± 0.01	3.03 ± 0.02	2.02 ± 0.01	0.45 ± 0.01	0.14 ± 0.01	$-1.03^{+0.09}_{-0.02}$	0.44
4310	21.98 ± 0.01	2.24 ± 0.06	0.78 ± 0.01	0.4 ± 0.07	0.21 ± 0.02	<-3.0	0.24
4406	23.2 ± 0.02	2.33 ± 0.08	4.2 ± 0.14	0.0 ± 0.0	0.13 ± 0.01	$-0.12^{+0.20}_{-0.20}$	1.04
4705	22.08 ± 0.01	0.94 ± 0.01	2.58 ± 0.01	0.0 ± 0.0	<0.1	$0.21^{+0.01}_{-0.01}$	0.82
5149	21.84 ± 0.01	3.28 ± 0.05	1.17 ± 0.0	0.8 ± 0.04	<0.1	$-1.97^{+0.20}_{-0.02}$	0.33
5415	21.45 ± 0.02	7.39 ± 0.12	1.8 ± 0.03	1.0 ± 0.0	<0.1	$-0.53^{+0.06}_{-0.06}$	0.54
5503	—	—	—	—	—	$0.49^{+0.01}_{-0.01}$	—
5509	22.1 ± 0.01	2.37 ± 0.04	4.26 ± 0.07	0.71 ± 0.03	<0.1	$-1.29^{+0.11}_{-0.01}$	0.91
5530	21.91 ± 0.01	3.23 ± 0.06	0.98 ± 0.0	0.66 ± 0.02	<0.1	$-2.04^{+0.04}_{-0.12}$	0.28
5534	—	—	—	—	—	$0.30^{+0.01}_{-0.01}$	—
5556	21.35 ± 0.01	3.26 ± 0.03	1.75 ± 0.01	0.79 ± 0.03	<0.1	$-2.52^{+0.02}_{-0.01}$	0.51
5564	21.53 ± 0.01	2.34 ± 0.02	1.8 ± 0.01	0.51 ± 0.03	<0.1	$-2.15^{+0.13}_{-0.13}$	0.44
5860	21.32 ± 0.01	2.34 ± 0.02	4.61 ± 0.03	0.57 ± 0.02	<0.1	$-0.25^{+0.05}_{-0.05}$	0.89
5974	22.44 ± 0.01	1.6 ± 0.02	3.81 ± 0.05	0.0 ± 0.0	0.12 ± 0.01	$0.61^{+0.02}_{-0.02}$	1.22
6071	21.45 ± 0.01	2.32 ± 0.02	4.56 ± 0.05	0.32 ± 0.02	<0.1	$-0.05^{+0.09}_{-0.09}$	1.02
6193	20.69 ± 0.01	3.48 ± 0.05	2.49 ± 0.03	0.5 ± 0.03	0.10 ± 0.01	$-0.24^{+0.03}_{-0.03}$	0.53
6224	21.63 ± 0.01	5.69 ± 0.11	5.01 ± 0.15	0.57 ± 0.02	<0.1	$-0.23^{+0.07}_{-0.07}$	1.58
6352	21.19 ± 0.01	2.46 ± 0.02	1.17 ± 0.0	0.61 ± 0.01	<0.1	$-0.15^{+0.10}_{-0.10}$	0.37
6572	22.01± 0.01	3.44 ± 0.07	6.36 ± 0.17	0.14 ± 0.01	0.12 ± 0.01	$0.28^{+0.13}_{-0.13}$	1.86
6647	22.05 ± 0.01	1.69 ± 0.03	1.27 ± 0.01	0.37 ± 0.02	<0.1	<-3.0	0.36
6898	21.28 ± 0.01	6.52 ± 0.14	0.62 ± 0.01	1.0 ± 0.0	0.5 ± 0.01	$-0.46^{+0.08}_{-0.08}$	0.12
7077	21.29 ± 0.01	4.79 ± 0.1	3.47 ± 0.08	0.39 ± 0.01	0.18 ± 0.01	$-0.34^{+0.03}_{-0.03}$	0.85

Table 3 – *continued*

ID	mag (AB)	n	$R_{e,\,circ}$ (kpc)	B/T	PSF/T (sS+PSF)	$\log\frac{sSFR}{sSFR(MS)}$	$\frac{R_{e,circ}}{R_0}$
7116	21.8 ± 0.01	1.36 ± 0.02	4.63 ± 0.06	0.1 ± 0.02	<0.1	$-0.24^{+0.15}_{-0.15}$	1.26
7491	21.53 ± 0.01	6.09 ± 0.15	0.88 ± 0.01	1.0 ± 0.0	<0.1	<-3.0	0.26
7617	21.6 ± 0.01	4.09 ± 0.1	1.93 ± 0.03	0.36 ± 0.02	0.22 ± 0.01	<-3.0	0.60
7923	22.07 ± 0.01	1.65 ± 0.08	0.7 ± 0.01	0.0 ± 0.0	0.27 ± 0.05	$-2.26^{+0.14}_{-0.06}$	0.20
8121	21.13 ± 0.01	2.61 ± 0.04	2.74 ± 0.04	0.15 ± 0.01	0.15 ± 0.01	$-1.96^{+0.02}_{-0.13}$	0.55
8569	20.73 ± 0.0	1.34 ± 0.06	4.74 ± 0.48	0.0 ± 0.0	<0.1	$-0.20^{+0.03}_{-0.03}$	1.00

Note. [a]Lens galaxy candidate. We show here the results inferred by masking out the ring, as detailed in Section 5.3. Without masking the ring, we obtained: mag=21.65 ± 0.02, n = 3.80 ± 0.08, $R_{e,\,circ}$ = 5.80 ± 0.17, B/T = 0.2 ± 0.01, PSF/T(sS+PSF) = 0.13 ± 0.01, $\log\frac{sSFR}{sSFR(MS)}$ = $-0.6^{+0.08}_{-0.06}$, $\frac{R_{e,circ}}{R_0}$ = 1.78.
The total magnitude, Sersic index, and circularized effective radius are from the single-Sérsic fit (see Section 5.1). For each object we also report the Bulge to Total flux ratio (B/T) from the composite Bulge+Disk model, discussed in Section 5.2, and the fractional contribution to the total flux of a hypothetical central point-source added to the single-Sérsic fit, PSF/T(sS+PSF), when it is >10%. The last two quantities are the distance from the MS in log-scale, as shown in Figures 5–8, and the distance from the $M_* -$size relation of local ETGs, shown in Figures 6, and 8.
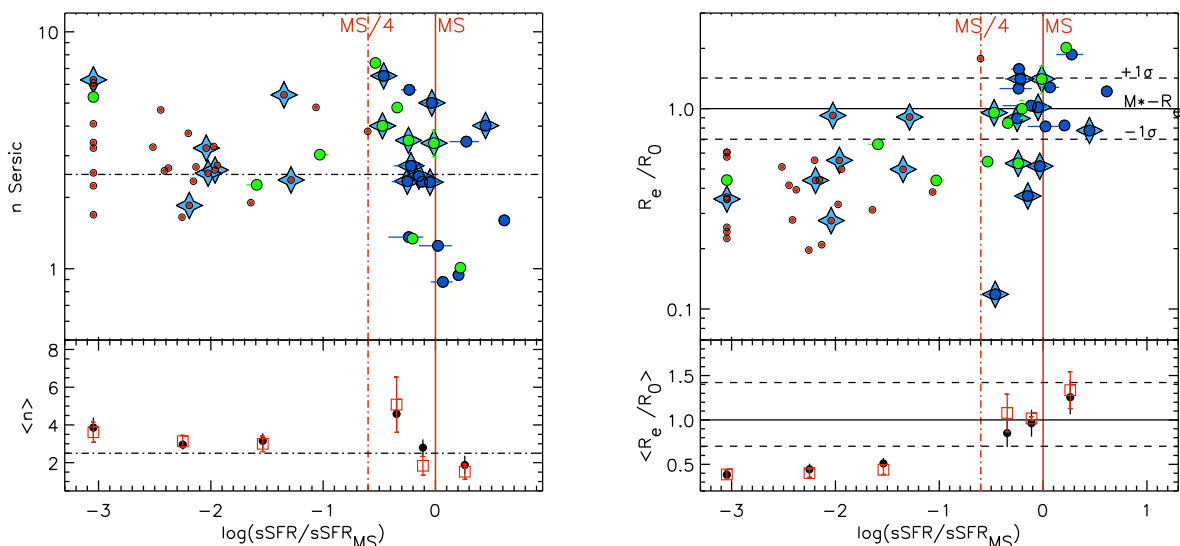
Figure 6. Left: Sérsic index versus distance from MS (i.e.log(sSFR/sSFR$_{MS}$)). The vertical red dot–dashed line at log(sSFR/sSFR$_{MS}$) = -0.6 marks the lower boundary of the MS band, and the horizontal $n = 2.5$ line separates disc-dominated and bulge-dominated objects. Right: the 'distance' from the M_*–R_e relation for local ETGs (horizontal solid line), expressed as R_e/R_0, as a function of the distance from MS, log(sSFR/sSFR$_{MS}$). Symbols are like in the previous figures. Bottom panels: mean values of the same quantities, in log(sSFR/sSFR$_{MS}$) bins chosen so to have 7–11 objects per bin. Black filled circles are relative to all the objects within a bin, while red open squares are obtained by only considering galaxies without evidence of AGN.

in size with respect to the objects quenched at higher redshifts. However, the small size of the sample prevent us from providing new clues on this issue.

5.2 Bulge–Disc decomposition

We built two-component bulge+disc models, by fitting each galaxy with two Sérsic components with $n = 1$ (disc) and $n = 4$ (bulge), both centred on the position derived in the previous single-Sérsic fit. The bulge to total flux ratio (hereafter, B/T) gives an indication of the relevance of the bulge-component in the galaxy. We discarded those models in which unreliable parameter values were retrieved for some of the subcomponents, i.e. too large/too small effective radius ($R_e > 4.0$ arcsec or $R_e < 0.03$ arcsec), or axis ratio $b/a < 0.1$. In most cases, the component with unreliable parameters was also found to contribute less than 10 per cent to the total flux (see Bruce

et al. 2012, for a similar discussion). In summary, beyond the three objects with irregular morphology, the double-component model was discarded for 15 galaxies, of which 10 are classified as simple discs (B/T = 0), and five as simple bulges (B/T = 1), (see Table 3). In Fig. 7, we show the relation between the B/T and the single-Sérsic n parameter for our sample (colour-coded as in the previous figures). Since Bruce et al. (2012) also studied bulge+disc decomposition for similarly massive galaxies ($M_* > 1.7 \times 10^{11}$ M$_\odot$, Salpeter IMF) at $1 < z < 3$, for comparison, we also show in the figure objects included in the same redshift and mass range from that sample (black small points). As in the Bruce et al. (2012) sample, also for our galaxies there is a good correspondence between the morphological classification based on the single-Sérsic index, n, and on B/T, although with a considerable scatter. In general, objects with B/T≥0.5 show $n \geq 2$–2.5, and those with $n < 2$–2.5 show B/T < 0.5. However, there are also some objects with a high n and B/T<0.5, i.e. located in the bottom-right quadrant of Fig. 7.
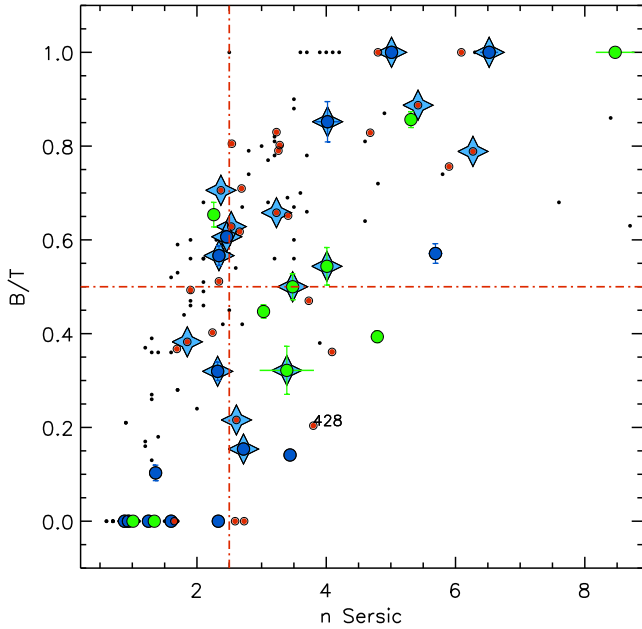
Figure 7. B/T versus n Sérsic. Symbols are like in the previous figures. The Bruce et al. (2012) results for objects in the same mass and redshift range of our sample are also shown for comparison (small black dots).

Some of these objects have a relatively high $0.3 \lesssim$ B/T $\lesssim 0.5$, still consistent with the presence of a significant bulge, as suggested by their high Sérsic index. For the remaining objects (two PACS-d galaxies, i.e.#3066, and #6572, and three MIPS-u galaxies, i.e. #1084, #1187, #8121) the apparent incongruity between n and B/T may be due to the presence of an unresolved point-like source in the centre, interpreted as a small bulge in the two-component fit ($R_{eBulge} < 1$ pixel), that could also be due to residual star formation or an AGN in the centre. This alternative is supported by the fact that when the SB profiles of these galaxies are fitted with a single-Sérsic model + central PSF, the resulting Sérsic index is $n \sim 1$ (a pure disc), and the point-like component is found to contribute ≥ 10 per cent of the total galaxy flux (see Table 3). Then, #428 (flagged in the figure) is the already mentioned lens galaxy candidate (also highlighted in Fig. 4, see also Section 5.3). In this case, the low B/T could be explained by the presence of the magnified background source, in the outer part of the galaxy, fit as a relatively bright disc.

The top panel of Fig. 8 shows the bulge to total light ratio B/T versus log(sSFR/sSFR$_{MS}$) in logarithmic scale, and the bottom panel the average trend, ⟨B/T⟩, as in Fig. 6. As mentioned for the n index, most of the *quenched galaxies* have B/T > 0.5, while the MS *galaxies* again split in two groups with B/T < 0.5 (64 per cent) or >0.5 (36 per cent) (when considering a boundary of B/T $= 0.3$ they split almost in half). For galaxies within the MS band ⟨B/T⟩ seems to increase with decreasing log(sSFR/sSFR$_{MS}$) (from ~0–0.2 at log(sSFR/sSFR$_{MS}$ > 0, to 0.5–0.7 at log(sSFR/sSFR$_{MS}$ < 0), and then to remain almost constant below it, where almost all the galaxies are bulge dominated. Figs 7 and 8 show that the high single-Sérsic index measured for all the secure AGNs on the MS appears to be due to the presence of a significant bulge component (B/T ≥ 0.3–0.5) in almost all of them (9/10). The only AGN with B/T < 0.3 is #3066, already discussed above. Since for most of the X-ray detected AGNs in our sample the nuclear emission does not dominate the photometric light in the optical-near-IR SED of the host galaxy, we expect a similarly low contamination also in the SB profile. However, to rule out the possibility that the nuclear emission
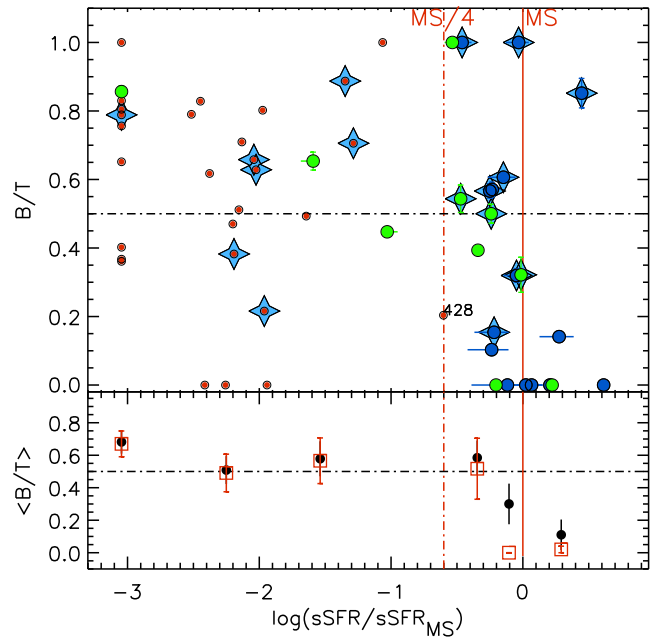

Figure 8. B/T versus distance from MS, log(sSFR/sSFR$_{MS}$). Symbols are like in the previous figures. Bottom panel: mean B/T ratio in bins of log(sSFR/sSFR$_{MS}$), as in Fig. 6. Black filled circles are relative to all the objects within a bin, and red open squares are obtained by excluding the AGNs.

have biased the results towards higher Sérsic indices and B/T ratios, we also tried to fit each object by adding a central point-source to the double component fit (i.e. bulge+disc+PSF). For most of the galaxies (50/56), the hypothetical point-source was found to contribute <10 per cent to the total flux. Moreover, the B/T ratio derived from the three-components fit (bulge+disc+PSF) agrees very well with that derived from the two-components fit (bulge+disc), for all the objects (including the X-ray detected AGNs). This means that the nuclear emission, if present, does not appreciably affect the light profile of our galaxies. The only exception may be represented by the two 'IRAC power-law' sources, i.e. #1906, and #6898, already discussed in Sections 4.2, and 5.1. Their compact size, high Sérsic n, and the fact that unreliable parameters were recovered for the disc component, both in the Bulge+Disc, and in the Bulge+Disc+PSF fits (B/T $= 1$), seems to suggest that their light profile is outshined by the nuclear emission. Hence we cannot reliably estimate their morphological parameters. However, for all the other AGNs, we conclude that a real link should exist between the presence of an AGN and a relevant bulge component in the host galaxy. This fits well with the notion that galaxies and SMBH grow together in order to establish the SMBH–bulge mass relation as observed in the local Universe (e.g. Magorrian et al. 1998; Ferrarese & Merritt 2000; Daddi et al. 2007b). The above analysis confirms that *MS galaxies* with $M_* \geq 10^{11}$ M$_\odot$ show on average a more relevant bulge component with respect to their lower mass counterparts (Bruce et al. 2014; Lang et al. 2014; Tacchella et al. 2014b). Moreover, since the most massive among star-forming galaxies are the first to be quenched, this supports the idea that the *mass quenching* processes is strongly related to the bulge growth and to AGN activity, as also assumed by some theoretical and semi-analytical models (Silk & Rees 1998; Di Matteo, Springel & Hernquist 2005; Somerville et al. 2008). This scenario is further supported by the large fraction of AGNs that we found also among quenched galaxies, as discussed in Section 6.
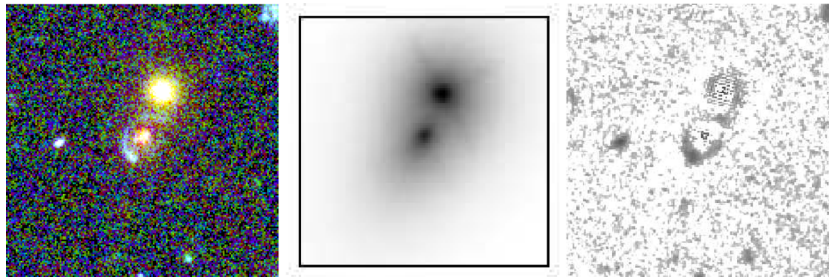
Figure 9. From left to right we show : the RGB image (where $R = H$-band ($F160W$), $G = z$-band ($F850LP$), B-band ($F435W$) of HST), the GALFIT model in the $F160W$ filter for single-Sérsic fit, and the residual (image-model) in the same filter for objects #427 and #428.
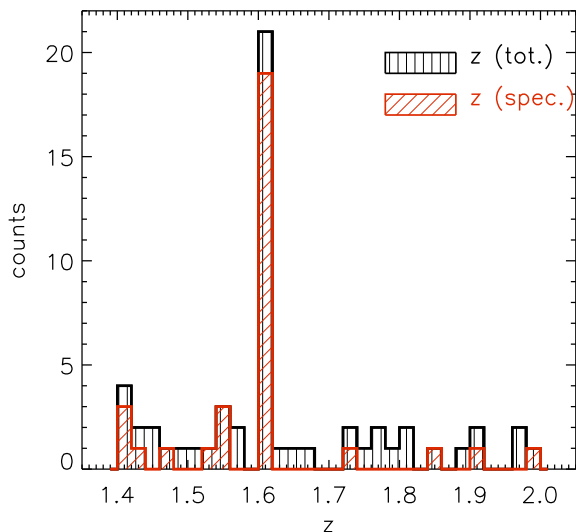

Figure 10. Redshift distribution of the sample. The diagonal-shaded red histogram shows the distribution for spectroscopic redshift only, whereas the vertical-shaded distribution refers to the addition of galaxies with only photometric redshift.

5.3 A double lens system?

The close pair of galaxies #428 and #427 represents a puzzling system as illustrated in Fig. 9 and we suspect that they may form a double lens system. The red, compact galaxy #428 is surrounded by a blue arc, which is highly reminiscent of a section of an Einstein ring, as illustrated in the left-hand panel of the figure. If this is indeed a lensing system, the very massive ETG #427, may contribute to further distort the image of a background source.

Object #427 at $z_{spec} = 1.427$ is spectroscopically classified as a passively evolving galaxy based on the CaH+K, MgII, and MgI absorption lines (Vanzella et al. 2008, see Table 1), while no spectroscopic confirmation exists for #428 which has a $z_{phot} = 1.59$. The small projected distance (1.88 arcsec, i.e. ∼16 kpc at this redshift) and the massive nature of the two galaxies makes it possible that they are a gravitationally bound pair at $z = 1.427$. The central spheroid of #428 is undetected in the U band and close to the detection limit in the HST/ACS B band, while the outer arc is detected in all bands, hence it is not a U-band *dropout*. If indeed lensed, the source should be at $2 \lesssim z \lesssim 3$. The radius of the blue arc is $R_{arc} = 0.8$ arcsec, somewhat larger than expected for the Einstein radius of an isolated $M_{tot} \sim 40 \times 10^{11}$ M$_\odot$ lens at $z = 1.427$ and a $z \sim 2$–3 background source, for which the Einstein radius would be $R_E = 0.33$ arcsec– 0.6 arcsec. This is assuming a dark matter contribution ∼40 times

the stellar mass of the galaxy. Hence, the unusual configuration of the system, with only half visible ring around object #428 (and such large R_E), could be due to the presence of the massive #427 neighbour perturbing the gravitational field and producing a warped and atypical source image.

The further exploration of the various components of this system has been pursued by fitting the SB distribution of #428 and #427 with both single-Sérsic function and with bulge+disc models (Section 5). From the single-Sérsic fit, we obtained a high Sérsic-index ($n = 3.8$) and a relatively large $R_{e,\,circ}$ (5.8 kpc) for #428, and $n = 2.73$ and $R_{e,\,circ} = 2.4$ kpc for #427. The corresponding model is shown in the middle panel of Fig. 9. Once the single-Sérsic models have been subtracted, strong ring-like residuals are visible in the outskirts of both galaxies as shown in the right-hand panel of Fig. 9. From this figure, it also appears that the bottom-right part of the blue ring of #428 emerges in the residual image, with an evident brighter 'blob' SE of the galaxy. A smaller ring also appears in the residual image of #427, along with a structure apparently bridging these two rings. The bulge+disc decomposition resulted in a very faint and small bulge ($B/T \sim 0.2$, $R_{e,circ,bulge} \sim 0.5$ kpc) for #428, and a bright and large disc $R_{e,\,circ,\,disc} \sim 5.2$ kpc), but produced similarly strong residuals. This shows that an exponential disc is not suitable to fit the outer structure in #428.

Thus, from these evidences we cannot conclude whether we are dealing with a double-lens system, or whether this complex structures are the result of tidal interactions. What is more certain is that the blue ring is a distinct, star-forming galaxy, either being lensed or torn apart by #428. We then derived more reliable morphological parameters and total photometry for the supposed lens galaxy by masking-out on the HST H-band image the outer arc with an annulus of internal and external radii of $r_{in} = 0.6$ arcsec and $r_{out} = 1.2$ arcsec, respectively. By fitting again the galaxy with a single-Sérsic function, we then derived nearly the same Sérsic index, ($n \sim 3.8$), but a smaller effective radius, $R_{e,\,circ} = 3.9$ kpc. Using the same masking, we have also determined the total magnitudes in all the other available HST optical (i.e. B,V,i,z) and near-IR (Y,J) filters and all the other GALFIT parameters to those derived in the H band. As shown in the Appendix (Fig. A1), a blended detection at MIPS/24 μm is also associated with the system with the MIPS peak being clearly shifted towards SE with respect of both the IRAC and the HST/WFC3 centroids. Hence, the 24 μm flux most likely comes from the blue arc, rather than from either of the two galaxies #427 and #428, confirming their quenched nature.

We fit the new HST optical/near-IR photometry with an SED including relatively low reddening ($A_V < 1$), as inferred from the MIPS upper limit (assuming MIPS non-detection, cf. Section 4.2, and Fig. 3). The derived sSFR (log(sSFR/sSFR$_{MS}$) = -1.4) is consistent with that of a purely quenched galaxy. Whatever the

6 AGN AND QUENCHING

Out of the 56 massive galaxies in this study, 18 (or 17) are hosting an AGN, as revealed by their X-ray and radio detection (cf. Section 3.3). This fairly high ∼30 per cent fraction is not uncommon among massive galaxies at these high redshifts (e.g. Daddi et al. 2007b; Fiore et al. 2009). AGN-driven, high velocity nuclear outflows are found to be ubiquitous among massive ($\gtrsim 10^{11}$ M$_{\odot}$) star-forming, near-MS galaxies (Förster Schreiber et al. 2014; Genzel et al. 2014). Given their extension (few kpc) such outflows must have fairly long lifetimes ($\gtrsim 10^8$ yr) and therefore be detectable even if the powering AGN is caught in an off phase, due to its short term variability. This may provide further evidence for SMBHs being responsible for regulating the growth of the galaxies and vice versa. It also provides circumstantial support to the notion of AGN feedback as a plausible physical process leading to mass quenching. However, evidence of AGN feedback, e.g. in the form of fast nuclear outflow, is not necessarily evidence for AGN quenching, as pointed out in the introduction.

Particularly interesting is the fact that the AGN fraction is quite high not only among MS galaxies (10–11/25, ∼40 ± 10 per cent) but also among sub-MS galaxies, which are either quenching or already quenched (7/31 ∼22 ± 7 per cent). One would have expected that fading of star formation should be accompanied by fading of nuclear activity as well. Why this is not the case? One possibility is the following. Galaxies may be quenched because at some point they are evacuated of virtually all their gas content, or gas supply from the circumgalactic medium is somehow suppressed. Yet, this does not mean they will remain gas free forever: even in absence of gas infall from the environment. The mere gas return from dying stars is sufficient to replenish the gas reservoir of galaxies over relatively short time-scales, with gas accumulating in the potential well. Even if supernovae of Type Ia may provide enough energy to drive galactic winds and outflows in less massive galaxies, in the most massive quenched galaxies the gas accumulation leads inevitably to a central cooling catastrophe and the establishment of an inflow towards the centre (Ciotti et al. 1991). What happens as a result of such a runaway cooling has been explored with hydrodynamical simulations by Ciotti & Ostriker (1997, 2001) and more recently by Novak et al. (2012, and references therein). The cooling gas is found to feed the central SMBH and its radiative and mechanical feedback is able to temporarily revert the inflow into an outflow, possibly even restoring a global galactic wind. As the galaxy is evacuated of its gas, the AGN subsides and gas starts to accumulate again until the next cooling catastrophe takes place and another cycle begins. The duty cycle of this intermittent behaviour is shorter the higher the rate of mass return from dying stars, which decreases with increasing age of a stellar population. Thus, the galaxies with the youngest stellar populations among quenched galaxies, have the highest rate of mass return, and therefore the shortest AGN duty cycle. At least qualitatively, this scenario accounts for the high frequency (∼22 per cent) of AGN among the quenched/quenching galaxies in our sample. Actually, their low level of star formation, rather than to quenching, could also be due to minor star formation activity that may accompany the central cooling catastrophe. This intermitting AGN activity is actually necessary to keep quenched a galaxy once it has been quenched in the first place.

We point out that a large fraction of X-ray detected AGNs in quenched galaxies at $1.5 \leq z \leq 2.5$ has been also recently un-

covered by other authors (Olsen et al. 2013; Tanaka et al. 2013; Whitaker et al. 2013). In particular Olsen et al. (2013) found that the fraction of luminous AGN ($LX_{0.5-8\,\mathrm{keV}} > 3 \times 10^{42}$ erg s^{-1}) among quenched and star-forming galaxies with $M_* > 5 \times 10^{10}$ M$_{\odot}$ are comparable (i.e. 19 ± 9 per cent, and 23 ± 5 per cent, respectively) in the 464.5 arcmin^2 CDF-S survey, which currently provides the deepest 0.5–8 keV data. They also found an X-ray excess by stacking the X-ray undetected quenched galaxies, and claim that 70–100 per cent of them should host a high- or low-luminosity AGN ($LX_{0.5-8\,\mathrm{keV}} \sim 10^{42}$ erg], s^{-1}). The larger fraction of luminous X-ray AGNs that we found among star-forming galaxies, with respect to that among quenched galaxies, mostly depends on the different selection criteria that we used to separate the two classes, not only based on *UVJ* rest-frame colours, but also on the sSFR (cf. Section 4). By adopting a pure *UVJ* colour-criterion one finds that the luminous AGN fraction among quenched and star-forming galaxies, are ∼26 ±8 per cent, and 28 ±9 per cent, respectively, nearly as in Olsen et al. (2013).

In our massive sample at $1.4 \leq z \leq 2$, AGNs quenched galaxies only account for ∼5 ± 5 per cent of the total X-ray luminosity density. This finding agrees well with recent results from Rodighiero et al. (2015) at similar redshift, and Georgakakis et al. (2014) at $z < 1.2$, showing that the bulk of the accretion density of the Universe seems to be associated with normal star-forming (i.e. MS) galaxies. For MS galaxies, we estimated an average $\log(L_X/\mathrm{SFR}) = 41.62 \pm 0.08$, which is from 0.6 to 0.8 dex higher than the average values found by Mullaney et al. (2012b), and Rodighiero et al. (2015) for similarly massive MS galaxies at $z \sim 2$. This discrepancy comes from the average X-ray luminosity being derived by combining both detected and stacked X-ray signals, while here we only consider X-ray detected objects. A better agreement is found with the average L_X/SFR ratio derived by Rodighiero et al. (2015) for X-ray detected objects in their two higher mass bins (i.e. $\log(L_X/\mathrm{SFR}) = 41.35 \pm 0.05$, 41.38 ± 0.05, reported to a Salpeter IMF, Rodighiero, private communication). The residual discrepancy (∼0.3 dex) should be attributed to the different depths of the X-ray surveys in the GOODS and the Cosmic Evolution Survey (COSMOS) fields.

7 A LESSER IMPACT OF ENVIRONMENT ON QUENCHING AT $z = 1.4 - 2$

7.1 The $z \sim 1.61$ overdensity

According to the Peng et al. (2010b) phenomenological model, environment quenching is not expected to play a major role at the redshifts and stellar masses explored in this paper. The existence of a diffuse, and well-documented sheet-like overdensity at $z \sim 1.61$ on the entire GOODS-South field (Castellano et al. 2007; Kurk et al. 2009; Giavalisco et al. 2011) offers the opportunity to test this expectation by comparing the abundance of quenched galaxies, bulge-dominated galaxies, and X-ray detected AGNs, within and outside the overdensity. We note that Castellano et al. (2007) isolated a symmetric structure corresponding to the highest density peak, centred approximately at RA = 03$^\mathrm{h}$:32$^\mathrm{m}$:29$^\mathrm{s}$.28, DEC. = $-27°$:42′:35.99$''$\$, and with an extension of ∼3 × 3 Mpc comoving, embedded in such a wide wall-like or filamentary overdensity. They considered as possible members of such cluster-like structure only the objects within a square of side $2R_A$ (where $R_A = 2.14$ Mpc is the Abell radius).

Here, we consider as part of the overdensity all the galaxies with spectroscopic redshift in the range $1.6 \leq z_\mathrm{spec} \leq 1.62$ (19 sources),

or photometric redshift in the range $1.5 \leq z_{\text{phot}} \leq 1.7$ (eight sources, see Fig. 10). Then, we also tested the results by only considering objects in the highest density peak as in Castellano et al. (2007) (16 in total, 11 of which spectroscopically confirmed). The results are summarized in the following, where the fractions relative to the highest density peak are shown in parenthesis.

(i) The fraction of quenched galaxies (i.e. galaxies with $\log(\text{sSFR}/\text{sSFR}_{\text{MS}}) < -1$) within the overdensity is 59 ± 9 per cent (68 ± 12 per cent), which is comparable to the fraction at all other redshifts, outside the overdensity, which is 52 ± 9 per cent (50 ± 8 per cent).

(ii) The fractions of bulge-dominated objects ($B/T \geq 0.5$) within, and outside the overdensity are also comparable within the errors, being 59 ± 9 per cent (62 ± 12 per cent), and 41 ± 9 per cent (45 ± 8 per cent), respectively. They are also comparable to the fraction of bulge-dominated galaxies found by Bruce et al. (2012) in the same mass and redshift range, in the UDS field (55 ± 9 per cent at $1.4 \leq z \leq 2$, or 65 ± 9 per cent at $1.5 \leq z \leq 1.7$).

(iii) Out of our 18 X-ray detected AGN hosts, 12 (6) are in the overdensity, and 6 (12) in the field. The relative fractions of X-ray detected AGN are $\sim 44 \pm 9$ per cent (37 ± 12 per cent) within the overdensity and $\sim 20 \pm 7$ per cent(30 ± 8 per cent) in the field.

In the overdensity there appears to be a slightly higher fraction (at the $\sim 1\sigma$ level) of quenched, bulge-dominated and X-ray detected galaxies, but given that these properties correlate with each other we cannot claim to have unambiguously detected an environmental effect. Overall, this indicates a lesser role for *environment quenching* with respect to the *mass quenching* within the studied redshift and mass ranges, where no morphology–density relation is yet observed. Concerning the X-ray detected AGN, we found different results when considering the more diffuse sheet-like structure, and the highest density peak, since six AGNs are at a distance of ~ 8 arcmin–10 arcmin (~ 4–5 Mpc, southward) from the cluster centre identified by Castellano et al. (2007). This discrepancy is probably due to statistical uncertainties due to the small number of objects in our sample. So, our data do not allow us to establish whether or not the overdensity has an effect on the frequency of AGN activity, of the kind proposed by some authors (Ruderman & Ebeling 2005; Fassbender, Šuhada & Nastasi 2012).

8 DISCUSSION AND CONCLUSIONS

This paper is meant to be a step towards shedding new light on the physical process(es) responsible for the suppression of the star formation in the most massive galaxies at high redshift, leading to the build up of the high-mass end of the quenched population observed in the local Universe (i.e. the so-called *mass quenching*). To this purpose, we took advantage of the high-quality WFC3/*HST* near-IR imaging (CANDELS), as well as of the multiwavelength data (from X-ray to radio) available in the GOODS-S field, to study a mass-complete sample of galaxies at $1.4 \leq z \leq 2$ with $M_* \geq 10^{11}\,\text{M}_{\odot}$. At this cosmic epoch the SFR density and the AGN activity reached their peak and, at the same time, the quenching of star formation started to be very efficient in galaxies with mass $\gtrsim 10^{11}\,\text{M}_{\odot}$. Hence, we chose this mass and redshift ranges so to deal only with galaxies which are either already quenched, or which have initiated the quenching process or soon will do so. The purpose is indeed to study the interconnection between *mass quenching*, and AGN, star formation activity, and morphology, especially with the aim at identifying transition objects that have left the MS since a short time. Such

transition objects are certainly rare compared to fully star-forming, MS galaxies or fully quenched ones, hence simple automatic criteria for identifying them are likely to be contaminated by these more common neighbours.

Although many studies have been performed in similar mass and redshift ranges, most of them were based on very large samples, which while providing statistical significance could lead to miss relevant information if automated procedure are used for the analysis. Instead in this work we study galaxies one by one, so to reliably derive their sSFR by addressing blending problems in mid-/far-IR data, and comparing results from different diagnostics. The studied sample consists of 56 galaxies, culled from the *K*-selected D07 optical-to-IRAC catalogue, so to include all the galaxies with $M_* \geq 10^{11}\,\text{M}_{\odot}$ (Salpeter IMF) and spectroscopic or photometric redshifts at $1.4 \leq z \leq 2$. The optical/IRAC data were complemented with *Spitzer*/MIPS and *Herschel*/PACS/SPIRE data. The main results can be summarized as follows.

(i) By comparing MIPS and high-resolution *HST* images, we identified sources which are blended in *Spitzer* data, and used $F160W$/WFC3/*HST* prior positions to estimate the amount of flux associated with each blended galaxy. We found that the automated MIPS counterpart association based on IRAC priors had failed for 7/56 (~ 12 per cent) sources, which had been erroneously considered as MIPS-detected, or, just in one case, MIPS-undetected. Based on these results, we derived the relative fractions of objects which are PACS-detected (PACS-d, 18/56), MIPS-detected/PACS-undetected (MIPS-d, 10/56), and MIPS/PACS-undetected (MIPS-u, 28/56). While ~ 12 per cent may appear a small contamination, it is worth emphasizing that these reclassified galaxies represent almost the totality of potential transition/quenching objects in the sample.

(ii) We examined the position of our galaxies on the M_*–SFR plane, relative to the MS of star-forming galaxies at $\langle z \rangle = 1.7$ (the mean redshift of the sample), formally including all the galaxies with an sSFR within a factor of 4 above and below the average relation (the 'MS band arcmin'). To accurately establish the 'degree of quenching' of each object, we first derived the SFR as the sum of the UV and IR contributions (SFR(IR+UV)), and then cross-checked the results using optical-to-IRAC SEDs, and two-colours BzK and UVJ diagrams. Consistently with the idea that the *mass quenching* process is more efficient in the most massive galaxies, we observe a turn down of the average SFR at such high masses. In fact, 31/56 galaxies (~ 55 per cent) are located below the lower boundary of the 'MS band', and 2/3 of the MS galaxies lie below the average M_*–SFR relation. All the galaxies below the 'MS band' turned out to have a sSFR more than 10 times lower with respect to the average relation ($\log(\text{sSFR}/\text{sSFR}_{\text{MS}}) < -1$), as well as properties typical of already *quenched* objects, such as SED, colours and spectra, when available. This suggests that the *mass quenching* may be a very fast process in massive galaxies, being able to shut down the star formation in relatively short time-scales ($\ll 1$ Gyr), though a much bigger sample should be analysed in a similar fashion to achieve firmer conclusions in this respect.

(iii) We fitted the SB of galaxies with both a single-Sérsic function and with a double Sérsic, in the latter case to model bulge+disc profiles. We found that the B/T, used as a proxy for the importance of the bulge component in a galaxy, provides results in general agreement with those obtained from the single-Sérsic index (n). In the full sample ~ 68 per cent of the objects have a relevant bulge component ($B/T > 0.3$), and ~ 50 per cent are bulge-dominated ($B/T > 0.5$). These findings are in agreement with recent results from Bruce et al. (2012, 2014), showing that while at $z > 2$ galaxies with

$M_* > 10^{11}$ M$_\odot$ are mostly disc-dominated, at $1 < z < 2$ they are primarily bulge+disc systems. In particular, ~84 per cent (26/31) of the quenched galaxies have a relevant bulge component, and 61 per cent (19/31) are bulge dominated. On the other hand, about half of the MS galaxies have B/T > 0.3, and ~36 per cent (9/25) are bulge-dominated. The average ⟨B/T⟩ seems to increase within the MS, with decreasing sSFR, and then remain almost constant below it. Although we do not have enough statistics to establish the solidity of this finding, this fits well with recent observational results showing that the bulge growth is directly related to the quenching of star formation (e.g. Genzel et al. 2014a; Lang et al. 2014; Tacchella et al. 2014b).

(iv) We identified 17 secure and one candidate AGN hosts in our sample (i.e.~30 per cent), both among MS (11/25, ~44 per cent) and among quenched (7/31, ~22 per cent) galaxies, by comparing the SFR derived from *Chandra*/X-ray and VLA/radio data with those inferred from IR+UV, and SED fitting. Although the fraction of AGNs among quenched galaxies is quite high, their contribution to the X-ray luminosity density is small, representing only 5 ± 5 per cent in our sample of $M_* \geq 10^{11}$ M$_\odot$ at $z = 1.4$–2, in agreement with recent results from Rodighiero et al. (2015). In general, we found that the presence of the AGN correlates with a steep central profile, with Sérsic $n \geq 2$–2.5, and B/T ≥ 0.3–0.5, not only in quenched galaxies, but also in almost all the MS galaxies. This is consistent with the idea that the galaxy bulge and the central SMBH grow together since early epochs, as expected based on the bulge mass–SMBH relation observed in the local Universe. Moreover, it seems that AGNs are much more frequent in galaxies with $-0.6 < \log(\text{sSFR/sSFR}_{\text{MS}}) < 0$ than in those with higher sSFR ($0 < \log(\text{sSFR/sSFR}_{\text{MS}}) < 0.6$), suggesting that the AGN is somehow related to the decline of the SFR. This findings provide some support to the notion that AGN feedback may be crucial in shutting down the star formation in the most massive galaxies, as assumed in some theoretical and semi-analytical models.

(v) With respect to the local ETGs, the majority of the quenched galaxies (28/31, ~90 per cent) are undersized (by a factor of ~ 2.5, on average), while the majority of the MS galaxies (20/25, ~ 80 per cent) are comparable to them in size, in agreement with what found in previous works. All the 5/25 compact MS galaxies are similar to the CSFG studied by Barro et al. (2013, 2014), showing high central concentration ($n > 2.5$, and B/T ≥ 0.5) and an sSFR slightly lower with respect to the average MS relation. Moreover, four out of five are AGN hosts, although in two objects the AGN dominates the photometric light, possibly affecting the derived galaxy size. All these characteristics suggest that these objects will be quenched soon, originating compact quenched remnants, as suggested by Barro et al.

(vi) In our sample 27 out of 56 galaxies are included in the well-known overdensity at $z = 1.61$ in the GOODS-S field, hence we compared the relative abundances of quenched galaxies, bulge-dominated (B/T ≥ 0.5) galaxies, and X-ray AGNs, within and outside the overdensity. This test showed that no appreciable difference exists in the relative fractions of these three sub-populations in the different environments. The result does not change significantly when the test is repeated by considering as part of the overdensity only the objects included in the highest density region (~3 × 3 Mpc) identified by Castellano et al. (2007). This suggests that the environment should have a minor (if not negligible) role in triggering the quenching of the star formation in the most massive galaxies at $z = 1.4$–2, as predicted by the Peng et al. (2010b, 2012) phenomenological model.

Perhaps the most relevant lesson learned from this *pilot* investigation is that careful object-by-object analysis is necessary to properly identify candidate galaxies on their way to be quenched, whose number and structure can be important for the identification of the physical mechanism(s) responsible for the quenching of star formation in massive high-redshift galaxies.

ACKNOWLEDGEMENTS

REFERENCES

Afonso J., Mobasher B., Koekemoer A., Norris R. P., Cram L., 2006, AJ, 131, 1216
Alonso-Herrero A. et al., 2006, ApJ, 640, 167
Avni Y., 1976, ApJ, 210, 642
Baldry I. K., Glazebrook K., Brinkmann J., Ivezić Ž., Lupton R. H., Nichol R. C., Szalay A. S., 2004, ApJ, 600, 681
Balestra et al., 2010, A&A, 512, 12
Barro G. et al., 2013, ApJ, 765, 104 (B13)
Barro G. et al., 2014, ApJ, 791, 52 (B14)
Bauer A. E., Conselice C. J., Pérez-González P. G., Grützbauch R., Bluck A. F. L., Buitrago F., Mortlock A., 2011, MNRAS, 417, 289
Berta S. et al., 2013, A&A, 551, A100
Bertin E., Arnouts S., 1996, A&AS, 117, 393
Béthermin M. et al., 2012, ApJ, 757, L23
Béthermin M., Wang L., Doré O., Lagache G., Sargent M., Daddi E., Cousin M., Aussel H., 2013, A&A, 557, A66
Bezanson R., van Dokkum P., van de Sande J., Franx M., Kriek M., 2013, ApJ, 764, L8
Birnboim Y., Dekel A., 2003, MNRAS, 345, 349
Bolzonella M., Miralles J.-M., Pelló R., 2000, A&A, 363, 476
Bongiorno A. et al., 2012, MNRAS, 427, 3103
Bruce V. A. et al., 2012, MNRAS, 427, 1666
Bruce V. A. et al., 2014, MNRAS, 444, 1660
Brusa M. et al., 2009, A&A, 507, 1277
Bruzual G., Charlot S., 2003, MNRAS, 344, 1000 (BC03)
Buitrago F., Trujillo I., Conselice C. J., Bouwens R. J., Dickinson M., Yan H., 2008, ApJ, 687, L61
Carollo C. M. et al., 2013, ApJ, 773, 112
Carollo C. M. et al., 2014, preprint (arXiv:1402.1172)
Cassata P. et al., 2010, ApJ, 714, L79
Cassata P. et al., 2013, ApJ, 775, 106
Castellano M. et al., 2007, ApJ, 671, 1497
Cimatti A. et al., 2004, Nature, 430, 184
Cimatti A. et al., 2008, A&A, 482, 21
Cimatti A. et al., 2013, ApJ, 779, L13
Ciotti L., Ostriker J. P., 1997, ApJ, 487, L105
Ciotti L., Ostriker J. P., 2001, ApJ, 551, 131
Ciotti L., D'Ercole A., Pellegrini S., Renzini A., 1991, ApJ, 376, 380
Croton D. J. et al., 2006, MNRAS, 365, 11
da Cunha E., Charlot S., Elbaz D., 2008, MNRAS, 388, 1595
Daddi E., Cimatti A., Renzini A., Fontana A., Mignoli M., Pozzetti L., Tozzi P., Zamorani G., 2004, ApJ, 617, 746 (D04)
Daddi E. et al., 2005, ApJ, 626, 680
Daddi E. et al., 2007a, ApJ, 670, 156 (D07)
Daddi E. et al., 2007b, ApJ, 670, 173
Daddi E. et al., 2010, ApJ, 713, 686
Damjanov I. et al., 2009, ApJ, 695, 101
de Barros S., Schaerer D., Stark D. P., 2014, A&A, 563, A81
Di Matteo T., Springel V., Hernquist L., 2005, Nature, 433, 604

Donley J. L., Rieke G. H., Pérez-González P. G., Rigby J. R., Alonso-Herrero A., 2007, ApJ, 660, 167
Elbaz D. et al., 2007, A&A, 468, 33
Elbaz D. et al., 2011, A&A, 533, A119
Epinat B. et al., 2009, A&A, 504, 789
Fassbender R., Šuhada R., Nastasi A., 2012, Adv. Astron., 2012, 32
Ferrarese L., Merritt D., 2000, ApJ, 539, L9
Fiore F. et al., 2008, ApJ, 672, 94
Fiore F. et al., 2009, ApJ, 693, 447
Fontana A. et al., 2004, A&A, 424, 23
Förster Schreiber N. M. et al., 2009, ApJ, 706, 1364
Förster Schreiber N. M. et al., 2014, ApJ, 787, 38
Fumagalli M. et al., 2014, ApJ, 796, 35
Genzel R. et al., 2011, ApJ, 733, 101
Genzel R. et al., 2014a, ApJ, 785, 75
Genzel R. et al., 2014b, ApJ, 796, 7
Georgakakis A. et al., 2014, MNRAS, 440, 339
Giavalisco M. et al., 2004, ApJ, 600, L93
Giavalisco M. et al., 2011, ApJ, 743, 95
Gobat R. et al., 2012, ApJ, 759, L44
González V., Labbé I., Bouwens R. J., Illingworth G., Franx M., Kriek M., Brammer G. B., 2010, ApJ, 713, 115
González V., Bouwens R., Illingworth G., Labbé I., Oesch P., Franx M., Magee D., 2014, ApJ, 781, 34
Granato G. L., De Zotti G., Silva L., Bressan A., Danese L., 2004, ApJ, 600, 580
Grazian A. et al., 2006, A&A, 449, 951
Grazian A. et al., 2007, A&A, 465, 393
Grogin N. A. et al., 2011, ApJS, 197, 35
Gunn J. E., Gott J. R., III, 1972, ApJ, 176, 1
Guo Y. et al., 2013, ApJS, 207, 24
Hickox R. C., Mullaney J. R., Alexander D. M., Chen C.-T. J., Civano F. M., Goulding A. D., Hainline K. N., 2014, ApJ, 782, 9
Hsu L.-T. et al., 2014, ApJ, 796, 60
Huertas-Company M. et al., 2013, MNRAS, 428, 1715
Ivison R. J. et al., 2010a, MNRAS, 402, 245
Ivison R. J. et al., 2010b, A&A, 518, L31
Karim A. et al., 2011, ApJ, 730, 61
Kellermann K. I., Fomalont E. B., Mainieri V., Padovani P., Rosati P., Shaver P., Tozzi P., Miller N., 2008, ApJS, 179, 71
Kennicutt R. C., Jr, 1998, ARA&A, 36, 189
Knobel C., Lilly S. J., Woo J., Kovač K., 2015, ApJ, 800, 24
Koekemoer A. M. et al., 2011, ApJS, 197, 36
Kurk J. et al., 2009, A&A, 504, 331
Kurk J. et al., 2013, A&A, 549, A63
Labbé I. et al., 2005, ApJ, 624, L81
Lang P. et al., 2014, ApJ, 788, 11
Larson R. B., Tinsley B. M., Caldwell C. N., 1980, ApJ, 237, 692
Longhetti M. et al., 2007, MNRAS, 374, 614
Luo B. et al., 2010, ApJS, 187, 560
Lutz D. et al., 2011, A&A, 532, A90
McGrath E. J., Stockton A., Canalizo G., Iye M., Maihara T., 2008, ApJ, 682, 303
Magdis G. E. et al., 2012, ApJ, 760, 6
Magnelli B., Elbaz D., Chary R. R., Dickinson M., Le Borgne D., Frayer D. T., Willmer C. N. A., 2009, A&A, 496, 57 (M09)
Magorrian J. et al., 1998, AJ, 115, 2285
Mancini C. et al., 2010, MNRAS, 401, 933
Maraston C., Pforr J., Renzini A., Daddi E., Dickinson M., Cimatti A., Tonini C., 2010, MNRAS, 407, 830
Martig M., Bournaud F., Teyssier R., Dekel A., 2009, ApJ, 707, 250
Mignoli M. et al., 2005, A&A, 437, 883
Miller N. A., Fomalont E. B., Kellermann K. I., Mainieri V., Norman C., Padovani P., Rosati P., Tozzi P., 2008, ApJS, 179, 114
Mineo S., Gilfanov M., Lehmer B. D., Morrison G. E., Sunyaev R., 2014, MNRAS, 437, 1698
Moore B., Katz N., Lake G., Dressler A., Oemler A., 1996, Nature, 379, 613
Mullaney J. R. et al., 2012a, MNRAS, 419, 95

Mullaney J. R. et al., 2012b, ApJ, 753, L30
Noeske K. G. et al., 2007, ApJ, 660, L43
Norris R. P. et al., 2006, AJ, 132, 2409
Novak G. S., Ostriker J. P., Ciotti L., 2012, MNRAS, 427, 2734
Oliver S. J. et al., 2010, A&A, 518, L21
Olsen K. P., Rasmussen J., Toft S., Zirm A. W., 2013, ApJ, 764, 4
Onodera M. et al., 2012, ApJ, 755, 26
Pannella M. et al., 2009, ApJ, 698, L116
Peng C. Y., Ho L. C., Impey C. D., Rix H.-W., 2010a, AJ, 139, 2097
Peng Y. et al., 2010b, ApJ, 721, 193
Peng Y.-j., Lilly S. J., Renzini A., Carollo M., 2012, ApJ, 757, 4
Perna M. et al., 2015, A&A, 574, A82
Poggianti B. M., Moretti A., Calvi R., D'Onofrio M., Valentinuzzi T., Fritz J., Renzini A., 2013, ApJ, 777, 125
Popesso P. et al., 2009, A&A, 494, 443
Pozzetti L. et al., 2007, A&A, 474, 443
Reddy N. A., Erb D. K., Steidel C. C., Shapley A. E., Adelberger K. L., Pettini M., 2005, ApJ, 633, 748
Reddy N. A., Pettini M., Steidel C. C., Shapley A. E., Erb D. K., Law D. R., 2012, ApJ, 754, 25
Renzini A., 2009, MNRAS, 398, L58
Rieke G. H. et al., 2004, ApJS, 154, 25
Rodighiero G. et al., 2011, ApJ, 739, L40
Rodighiero G. et al., 2014, MNRAS, 443, 19
Rodighiero G. et al., 2015, ApJ, 800, L10
Rosario D. J. et al., 2015, A&A, 573, A85
Ruderman J. T., Ebeling H., 2005, ApJ, 623, L81
Salim S. et al., 2009, ApJ, 700, 161
Salpeter E. E., 1955, ApJ, 121, 161
Saracco P., Longhetti M., Andreon S., 2009, MNRAS, 392, 718
Saracco P., Longhetti M., Gargiulo A., 2011, MNRAS, 412, 2707
Sargent M. T., Béthermin M., Daddi E., Elbaz D., 2012, ApJ, 747, L31
Schreiber C. et al., 2015, A&A, 575, A74
Sersic J. L., 1968, Atlas de galaxias australes. Observatorio Astronomico, Cordoba, Argentina
Shen S., Mo H. J., White S. D. M., Blanton M. R., Kauffmann G., Voges W., Brinkmann J., Csabai I., 2003, MNRAS, 343, 978
Silk J., Rees M. J., 1998, A&A, 331, L1
Somerville R. S., Hopkins P. F., Cox T. J., Robertson B. E., Hernquist L., 2008, MNRAS, 391, 481
Stark D. P., Schenker M. A., Ellis R., Robertson B., McLure R., Dunlop J., 2013, ApJ, 763, 129
Stott J. P., Collins C. A., Burke C., Hamilton-Morris V., Smith G. P., 2011, MNRAS, 414, 445
Szokoly G. P. et al., 2004, ApJS, 155, 271
Szomoru D., Franx M., van Dokkum P. G., Trenti M., Illingworth G. D., Labbé I., Oesch P., 2013, ApJ, 763, 73
Tacchella S. et al., 2014a, submitted
Tacchella S. et al., 2014b, preprint (arXiv:1411.7034)
Tacconi L. J. et al., 2010, Nature, 463, 781
Tanaka M. et al., 2013, PASJ, 65, 17
Toft S. et al., 2007, ApJ, 671, 285
Trujillo I. et al., 2006, ApJ, 650, 18
Trujillo I., Conselice C. J., Bundy K., Cooper M. C., Eisenhardt P., Ellis R. S., 2007, MNRAS, 382, 109
Valentinuzzi T. et al., 2010, ApJ, 712, 226
van der Wel A., Bell E. F., van den Bosch F. C., Gallazzi A., Rix H.-W., 2009, ApJ, 698, 1232
van Dokkum P. G. et al., 2008, ApJ, 677, L5
Vanzella E. et al., 2005, A&A, 434, 53
Vanzella E. et al., 2006, A&A, 454, 423
Vanzella E. et al., 2008, A&A, 478, 83
Whitaker K. E. et al., 2010, ApJ, 719, 1715
Whitaker K. E., van Dokkum P. G., Brammer G., Franx M., 2012, ApJ, 754, L29
Whitaker K. E. et al., 2013, ApJ, 770, L39
Williams R. J., Quadri R. F., Franx M., van Dokkum P., Labbé I., 2009, ApJ, 691, 1879

Williams C. C. et al., 2014, ApJ, 780, 1
Wuyts S. et al., 2007, ApJ, 655, 51
Wuyts S. et al., 2011, ApJ, 742, 96
Xue Y. Q. et al., 2011, ApJS, 195, 10

APPENDIX A: MIPS DEBLENDING

In this appendix, we detail the procedure used to derive the MIPS flux (and SFR) estimates for blended sources in our sample, whose results are shown in Section 4 and Fig. 2. Since the 24 μm/MIPS FWHM (=5.9 arcsec) is substantially larger than the size of our galaxies, each blended system includes all the objects closer than ∼3 arcsec (HWHM) to the centroid of the MIPS emission. We used GALFIT to decompose the blended sources by fitting PSF models on the fixed *F*160*W*/WFC3 positions, leaving the galaxy magnitude as the only free parameter to be recovered. To avoid to have residual flux in the neighbourhood, the sources at a distance 3–4 arcsec $< r <$ 20 arcsec from the galaxy(ies) of interest were also fit together, but fixing all the parameters (i.e. position and magnitudes) to the known values from the available MIPS catalogue. In the following, we discuss the results derived for each object, or pair (when both the galaxies in a blended pair are included in our sample). We considered as MIPS-detected (to be included in MIPS-d subsample) objects with SNR>3, and treated the others as upper limits (at 2σ or 3σ, for SNR<1 and $\geq$1, respectively).

(i) *Objects #427 and #428.* In the MIPS catalogue based on IRAC positions the MIPS counterpart had been wrongly assigned to #427, which is not compatible with such high MIPS flux, being spectro-scopically classified as ETG as proved by the CaHK, Mg$_{II}$, MgI absorption lines (GOODS) and lack of the O[II] emission line (ex-pected for a star-forming galaxy in the (VLT/FORS2) observed wavelength-range (Vanzella et al. 2008). Moreover, the results of
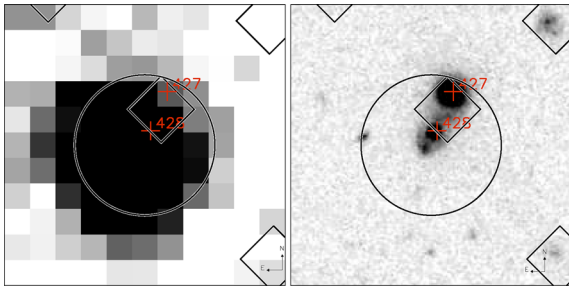

Figure A1. Comparison between MIPS/24 μm and *HST*/WFC3 *H*-band (*F*160*W*) images for objects #427 and #428. Both cutouts are 12 arcs in size. The red crosses correspond to WFC3/*HST* positions, while the large open circle shows the MIPS FWHM (5.9 arcsec), centred on the peak of the 24 μm/MIPS emission. The open diamonds mark the positions of IRAC sources in the field.
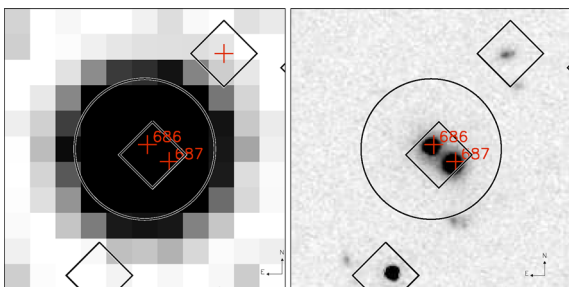

Figure A2. Same as Fig. A1, for objects #686 and #687.

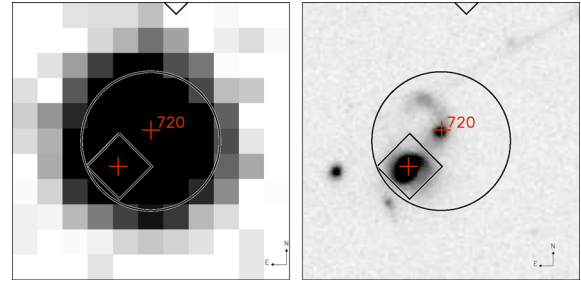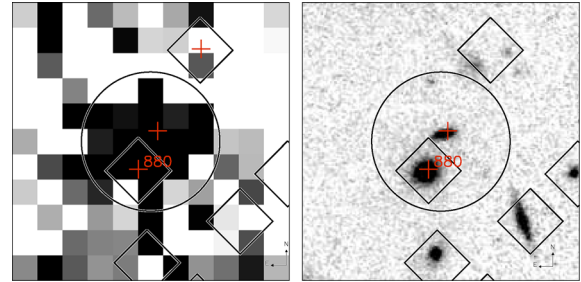**Figure A3.** Same as Fig. A1, for object #720.

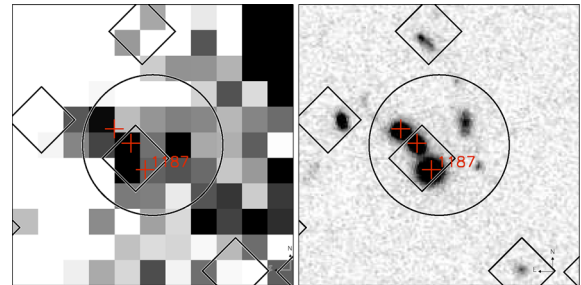**Figure A4.** Same as Fig. A1, for object #880.

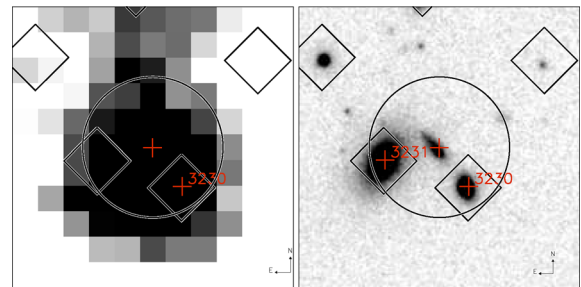**Figure A5.** Same as Fig. A1, for object #1187.

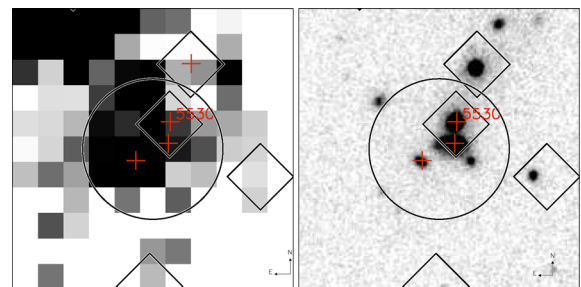**Figure A6.** Same as Fig. A1, for objects #3230 and #3231.

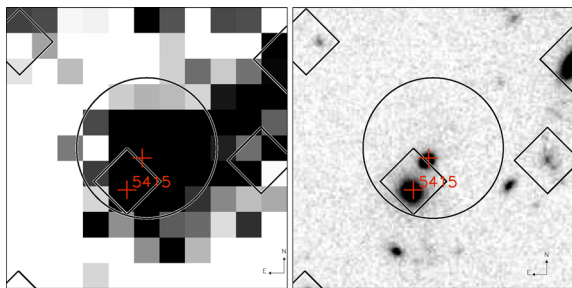**Figure A7.** Same as Fig. A1, for object #5530.

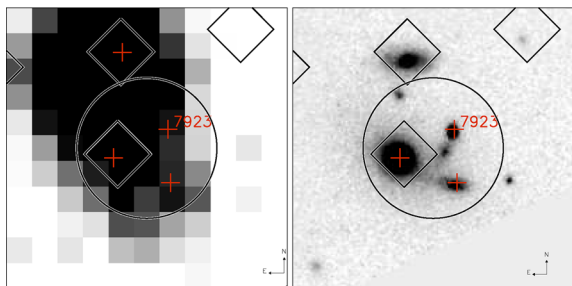**Figure A8.** Same as Fig. A1, for object #5415.

Figure A9. Same as Fig. A1, for object #7923.

PSF fitting on the image confirm that object #427 has a low 24 µm flux (F24< 26 µJy), while most of the MIPS flux should come from object #428. However, as detailed in Section 5.3, this is one of the most peculiar case of blending in our sample, being consistent with a double lens system. In this perspective, the MIPS flux should be associated with a lensed background star-forming galaxy, probably at $z \sim 2$–3.

(ii) *Objects #686 and #687*. These galaxies constitute a gravitationally bound system, as proved by their spectroscopic redshifts and mutual distance (Appendix B). The PSF fitting on the *HST*/WFC3 positions suggested that most of the MIPS emission comes from the AGN host #686, although a small percentage of the flux may be associated with the companion (#687). However, since both the red colours of #687, and the SED fitting results, suggest old age ($\sim$2 Gyr), and very low reddening ($A_V = 0.3$ mag), and SFR ($\sim$1 $M_\odot$ yr^{-1}), we considered this object as MIPS-u(cf. Table 2). We notice that, also if considered as MIPS-detection, #687 would remain a 'border-line' galaxy more than four times below the MS, since the MIPS flux derived from PSF fitting ($F_{24} = 65.2 \pm 13.8$ µJy) is very close to the quoted 3σ upper limit ($F_{24} < 59.76$ µJy).

(iii) *Object #720*. This galaxy has a near-IR/optical bright and massive ($M_* \sim 5 \times 10^{11} M_\odot$) neighbour (i.e. object #721), not included in our sample since its photometric redshift is slightly lower than the cut used in our sample-selection, i.e. $z_{phot} = 1.36$. In the GOODS catalogue #721 had been identified as the only counterpart of the bright MIPS source. On the contrary, our deblending procedure suggested that most of the MIPS flux should be associated with object #720 ($F_{24} = 204.4 \pm 9.4$ µJy), with a smaller fraction of the flux ($F_{24} = 83.5 \pm 10$ µJy) coming from #721. The presence of peculiar tidal tail seems to suggest that this could be also a merging system, but this hypothesis is not supported by spectroscopic information.

(iv) *Object #880*. The detection from the GOODS catalogue (SNR>3) was replaced with an upper limit, since the MIPS source seems to be the result of two blended marginal detection, as also suggested by the elongated shape of the source in the MIPS image.

(v) *Object #1187*. As for object #880, this MIPS detection appeared to be the sum of two or three blended partial detection's. Hence, the MIPS flux was replaced with an upper limit, consistently with the 'quenched nature' suggested by the optical/near-IR colours of the galaxy.

(vi) *Objects #3230 and #3231*. These objects are blended with a third lower-mass ($\sim$2 × 10^{10} $M_\odot$) neighbour (#3232, $z_{phot} \sim 2$), not included in the MIPS GOODS catalogue, which instead seems to be responsible of the majority of the MIPS flux ($F_{24} = 109.6 \pm 29.3$ µJy). As detailed in Appendix B, while the object in the middle could be just a projected neighbour, #3230 and #3231 are spectroscopically confirmed at the same redshift. As also proved by their spectra, #3230 and #3231 seems to be quenched galaxies, with MIPS fluxes < 46 µJy and < 62 µJy (sSFR$\lesssim 10^{-10}$yr^{-1}), respectively.

(vii) *Object #5530*. This MIPS source, previously considered as detected above 3σ, was decomposed in three different sources, based on the WFC3 positions. A marginal 2σ detection is found for the SE component, while the MIPS flux of #5530 is below the 2σ upper limit.

(viii) *Object #5415*. This galaxy was considered as MIPS-detected in the automated MIPS-source extraction procedure, based on IRAC priors. However, it is blended with a close object (i.e. #5414, at $z_{phot} = 1.96$, and not included in our sample because of its mass two times below the mass limit). The PSF fitting method reveals a secure MIPS detection (SNR$\sim$4) for the neighbour, and a marginal detection (SNR$\sim$2.5) for #5415. In this case, we classified #5415 as MIPS-d, due to its blue colours (typical of *sBzK* and blue star-forming *UVJ*), and to the SED fitting results, showing reddening $A_V \sim 1$, and SFR(SED) comparable with SFR(IR+UV), derived from MIPS (cf. Table 2).

(ix) *Object #7923*. This galaxy is part of a complex blended system, and does not have MIPS counterparts within 2 arcsec in the MIPS catalogue based on IRAC positions (the closest one is 2.4 arcsec away, SE, to this object). The MIPS flux decomposition based on WFC3 positions confirmed that this galaxies is not detected in MIPS, with a SNR<1, thus in Fig. 2 we replaced the 3σ upper limit with a 2σ upper limit.

APPENDIX B: CLOSE PAIRS, GROUPS, AND MERGERS

Since many projected pairs are included in our sample, for each galaxy we checked the redshift of all the closest neighbours (dist≤5 arcsec), to check if they are also gravitationally bound. As detailed below, some of the bound galaxy pairs in our sample are possibly included in the overdensity at $z \sim 1.61$. In the following, we summarize the results for the most probable cases, including (i) pairs with at least one member with spectroscopic redshift and a companion with consistent photometric redshift, (ii) pairs with two photometric redshifts in agreement within $\Delta z \sim 0.1$, or – just in one case – (iii) pairs with visible tidal tails, suggesting interaction, although the difference in photometric redshifts is $\Delta z > 0.1$.

(i) *#3231, #3230* are two MIPS-u galaxies with early-type morphology, at a projected distance of 3.62 arcsec, and spectroscopically identified at $z_{spec} = 1.610$ and $z_{spec} = 1.615$, respectively (Mignoli et al. 2005, i.e. K20 survey). There is a third bluer galaxy in the middle of this pair, with a photometric redshift of $z_{phot} = 2.09$, which is the closest counterpart for the 24 µm/MIPS source. Recently, Tanaka et al. (2013) identified these galaxies, together with the X-ray source #3258 in our sample (at $z = 1.605$, and 23 arcsec far from #3231), as likely members of an X-ray detected group of

8 galaxies, located ~ 5 arcmin (2.5 Mpc) away from centre of the highest density region in the overdensity at $z \sim 1.61$. Object #3231 has been recognized by the authors as the brightest group galaxy. It is interesting to note that its size is comparable to that of local ETGs with similar mass.

(ii) *#686 and #687*: The PACS-d #686 is classified as BLAGN/QSO-1 in the literature, and spectroscopically confirmed at $z = 1.617$ (Szokoly et al. 2004, see also table 1, and Section 3.3). The quenched companion #687 has an early-type morphology, lies at a projected distance of $d \sim 1.07$ arcsec and has a 'likely' spectroscopic redshift of $z_{\rm spec} = 1.609$ (Vanzella et al. 2008). Based on the criterion used in the previous section, these galaxies would be part of the highest density peak in the overdensity at $z = 1.61$. However, if both redshifts are correct, these objects would have a comoving radial distance of ~ 12 Mpc from each other, hence would not be interacting.

(iii) Kurk et al. (2009) identified a close triplet of galaxies, including *#986* ($z = 1.609$), indicated as the brightest confirmed galaxy member, *#1084* ($z = 1.614$), and *#880* ($z = 1.612$). All three objects are quenched/quenching ETGs, with the largest distance between them of 20.0 arcsec (169 kpc) and with the largest difference in redshift corresponding to ~ 575 km s^{-1}. They lie about 1.5 arcmin (i.e. 760 kpc) from the centre of the highest density region described by Castellano et al. (2007). Kurk et al. (2009) concluded that the relatively small crossing time of a galaxy in this triplet ($\sim 3 \times 10^8$ yr), indicates that they are possibly undergoing a merging.

(iv) The MIPS-u *#1187* galaxy ($z_{\rm phot} = 1.66$) has two very close companions. While the closest object at a projected distance of 1.27 arcsec has $z_{\rm spec} = 0.86$ (Vanzella et al. 2005, 2006, 2008), the second one (at a distance of 2.17 arcsec) has $z_{\rm phot} = 1.54$ (ID:GOODS-MUSIC-15228). This source seems to be a quenched galaxy (being also undetected at MIPS/24 µm), with red colours, and spheroidal morphology ($n = 2.33$, $R_{\rm e, circ} \sim 1.2$ kpc). Moreover, also a bluer, fainter galaxy (#1188 in the D07 catalogue) at $z_{\rm phot} = 1.57$ lies at a distance of 4.27 arcsec from #1187. Hence, it may be that these three galaxies are gravitationally bound, and may even be part of the overdensity at $z = 1.61$.

(v) The highly obscured PACS-d galaxy *#5534* with $z_{\rm spec} = 1.616$ has an asymmetric morphology indicative of a merging system. Moreover, it has a bluer neighbour at a distance of 3.02 arcsec, with $z_{\rm phot} = 1.59$ (ID:GOODS-MUSIC-6738).

(vi) Object *#720* ($z_{\rm phot} = 1.89$) shows a tidal feature towards the closest neighbour located at a projected distance of ~ 2 arcsec, which becomes even more evident when the derived 2D SB best-fitting model is subtracted to the real galaxy image (e.g. GAL-FIT residual image). The putative companion is a massive galaxy ($M_* \sim 5 \times 10^{11} M_\odot$) with visible spiral arms, with an insecure spectroscopic redshift $z_{\rm spec} = 2.49$ (Popesso et al. 2009), in disagreement with the photometric one, designed as the best solution, at $z_{\rm phot} = 1.43$ (ID:GOODS-MUSIC-16094). Difficult to say whether the two galaxies are a physical pair or not.

(vii) Objects *#427 and #428* represent the most peculiar pair in our sample, since it seems to be a double lens system, as detailed in Section 5.3. Although #427 is spectroscopically confirmed at $z = 1.427$ while #428 has a photometric redshift $z_{\rm phot} = 1.59$, they may represent an interactive pair, as suggested by the *bridge* between them as discussed in Section 5.3.

This paper has been typeset from a TEX/LATEX file prepared by the author.